

# Onset of a Large Ejective Solar Eruption from a Typical Coronal-Jet-Base Field Configuration

Navin Chandra Joshi<sup>1</sup>

*School of Space Research, Kyung Hee University, Yongin, Gyeonggi-Do, 446-701, Korea;  
navin@khu.ac.kr, njoshi98@gmail.com*

Alphonse C. Sterling<sup>2</sup>

*Heliophysics and Planetary Science Office, ZP13, Marshall Space Flight Center, Huntsville,  
AL 35812, USA*

Ronald L. Moore<sup>2,3</sup>

*Heliophysics and Planetary Science Office, ZP13, Marshall Space Flight Center, Huntsville,  
AL 35812, USA*

*Center for Space Plasma and Aeronomic Research (CSPAR), UAH, Huntsville, AL 35805,  
USA*

Tetsuya Magara<sup>1,4</sup>

*School of Space Research, Kyung Hee University, Yongin, Gyeonggi-Do, 446-701, Korea*

*Department of Astronomy and Space Science, School of Space Research, Kyung Hee  
University, Yongin, Gyeonggi-Do, 446-701, Korea*

Young-Jae Moon<sup>1,4</sup>

*School of Space Research, Kyung Hee University, Yongin, Gyeonggi-Do, 446-701, Korea*

*Department of Astronomy and Space Science, School of Space Research, Kyung Hee  
University, Yongin, Gyeonggi-Do, 446-701, Korea*

---

<sup>1</sup>School of Space Research, Kyung Hee University, Yongin, Gyeonggi-Do, 446-701, Korea

<sup>2</sup>Heliophysics and Planetary Science Office, ZP13, Marshall Space Flight Center, Huntsville, AL 35812, USA

<sup>3</sup>Center for Space Plasma and Aeronomic Research (CSPAR), UAH, Huntsville, AL 35805, USA

<sup>4</sup>Department of Astronomy and Space Science, Kyung Hee University, Yongin, Gyeonggi-Do, 446-701, Korea

## ABSTRACT

Utilizing multiwavelength observations and magnetic field data from *SDO/AIA*, *SDO/HMI*, *GOES* and *RHESSI*, we investigate a large-scale ejective solar eruption of 2014 December 18 from active region NOAA 12241. This event produced a distinctive “three-ribbon” flare, having two parallel ribbons corresponding to the ribbons of a standard two-ribbon flare, and a larger-scale third quasi-circular ribbon offset from the other two ribbons. There are two components to this eruptive event. First, a flux rope forms above a strong-field polarity-inversion line and erupts and grows as the parallel ribbons turn on, grow, and spread apart from that polarity-inversion line; this evolution is consistent with the tether-cutting-reconnection mechanism for eruptions. Second, the eruption of the arcade that has the erupting flux rope in its core undergoes magnetic reconnection at the null point of a fan dome that envelops the erupting arcade, resulting in formation of the quasi-circular ribbon; this is consistent with the breakout-reconnection mechanism for eruptions. We find that the parallel ribbons begin well before ( $\sim 12$  min) circular ribbon onset, indicating that tether-cutting reconnection (or a non-ideal MHD instability) initiated this event, rather than breakout reconnection. The overall setup for this large-scale (circular-ribbon diameter  $\sim 10^5$  km) eruption is analogous to that of coronal jets (base size  $\sim 10^4$  km), many of which, according to recent findings, result from eruptions of small-scale “minifilaments.” Thus these findings confirm that eruptions of sheared-core magnetic arcades seated in fan-spine null-point magnetic topology happen on a wide range of size scales on the Sun.

*Subject headings:* Sun: flare – Sun: activity – Sun: X-rays, gamma rays – Sun: magnetic field

## 1. Introduction

Solar flares, the most violent explosions on the Sun, are vigorous magnetic energy releases involving magnetic reconnection. The magnetic reconnection results in the formation of flare ribbons in the chromosphere and chromosphere-corona transition region, via the reconnection, a portion of the released energy is converted into kinetic energy of accelerated charged particles and another portion is converted directly into plasma thermal energy (see reviews by [Benz 2008](#); [Shibata & Magara 2011](#), and references cited therein). The reconnection starts in the corona, and flare-ribbon formation occurs in the chromosphere

immediately after the onset of the reconnection. The ribbon emission results from heating of the chromospheric plasma by the impact of accelerated charged particles/electrons that stream downward from the reconnection region along newly-reconnected field lines, and from heat conduction from the coronal plasma directly heated by the reconnection (see review by [Fletcher & Hudson 2001](#), and references cited therein). Solar flares can be classified as “confined” or “eruptive/ejective,” based respectively on whether they are or are not produced in tandem with a coronal mass ejection (CME). Several numerical simulation studies investigating the magnetic configuration/topology and the initiation/triggering processes of solar flares have been performed in two-dimensions (2D) and three-dimensions (3D)(see reviews by [Schmieder et al. 2015](#); [Janvier et al. 2015](#), and references cited therein).

One of the well-accepted models for ejective flares is based on a 2D picture and is called “CSHKP,” because it is due to a combination of investigations by [Carmichael \(1964\)](#), [Sturrock \(1966\)](#), [Hirayama \(1974\)](#), and [Kopp & Pneuman \(1976\)](#); this concept, sometimes augmented with additional findings, is also sometimes referred to as “the standard model for solar ejective flares/eruptions.” (In referring to this models for ejective flares/eruptions, we will use the terms “CSHKP” and “standard model” interchangeably in the remainder of the text.) According to this model, the flare reconnection occurs at a vertical current sheet underneath an erupting solar filament/flux rope in the core of a magnetic arcade. As the eruption and reconnection continue, the erupting filament/flux rope becomes progressively more magnetically unleashed from the photosphere and blows out the enveloping arcade to make a CME, while newly-reconnected field below the reconnection region forms strongly-emitting flare loops. Charged particles are accelerated at the reconnection site, and move upward and downward from that site. Those particles directed upward are in reconnected field added to the erupting flux rope. Downward-directed particles flow along the reconnected field lines forming the flare loops, and the chromospheric material in the flare-loop feet impacted by accelerated particles gets heated and appears as bright parallel flare ribbons on either side of the magnetic polarity inversion line (PIL) of the pre-eruption arcade. This kind of flare is commonly referred to as a “two-ribbon solar flare.” Flare events have been observed showing various features of this model (e.g., [Tsuneta et al. 1997](#); [Shibata 1999](#); [Benz 2008](#); [Joshi et al. 2013, 2016b](#), and references cited therein). This 2D CSHKP model alone however does not explain several 3D characteristics of solar flares, including the sigmoid structure of the erupting region, what initiates the eruption of the flux rope, the evolution of the flare loops from being initially nearly aligned with the PIL to being nearly normal to it, and other aspects. To explain these features, several 3D scenarios have been proposed ([Moore & Labonte 1980](#); [Shibata et al. 1995](#); [Moore et al. 2001](#); [Priest & Forbes 2002](#); [Shibata & Magara 2011](#); [Janvier et al. 2015](#)).

Apart from the parallel two-ribbon flares, flares with circular ribbons have also been

observed and studied (e.g., [Masson et al. 2009](#); [Su et al. 2009](#); [Reid et al. 2012](#); [Wang & Liu 2012](#); [Sun et al. 2013](#); [Jiang et al. 2013](#); [Wang & Liu 2014](#); [Jiang et al. 2014](#); [Vemareddy & Wiegelmann 2014](#); [Joshi et al. 2015](#)). This type of ribbon is believed to result from reconnection at the magnetic null in a typical fan-spine magnetic configuration. This configuration consists of inner and outer fan shells, with the inner shell being a closed dome of loops having one foot in a minority-magnetic-polarity region, and the outer shell being a dominant-magnetic-polarity canopy of far-reaching field sheathing the dome and forming a magnetic spine field that is open or connects to the solar surface at a remote location. These inner and outer fan regions are separated by a separatrix layer, resulting in a magnetic null between the top of the closed inner shell and the open outer shell (see Figure 1 of [Pariat et al. \(2009\)](#) and [Sun et al. \(2013\)](#)). As we will discuss further below, reconnection at the null plausibly results in the circular ribbon. Possibilities for driving magnetic reconnection at this null include eruption of an underlying filament/flux rope from low along the PIL of the closed-field dome ([Sun et al. 2013](#); [Jiang et al. 2013, 2014](#); [Joshi et al. 2015, 2016a](#)); and shearing of the dome field lines, making the dome field press on the null (e.g., [Vemareddy & Wiegelmann 2014](#)). Some studies also suggest that quasi-separatrix-layer reconnection in the top of the separatrix layer also can make circular-ribbon flares (e.g., [Reid et al. 2012](#)). There are only a few papers that deal with simulations of these kinds of eruptions and null-point reconnections ([Masson et al. 2009](#); [Török et al. 2009](#); [Pariat et al. 2009](#); [Jiang et al. 2013](#)).

From observations, we know that the eruption of a filament, sigmoid, and/or flux-rope structure plays a crucial role in driving solar flares. Several models have been suggested for this aspect of solar eruptions and flares. In the “tether-cutting” scenario ([Moore & Labonte 1980](#); [Sturrock et al. 1984](#); [Moore et al. 2001](#)), it was suggested that, initially, shearing and converging photospheric flow brings opposite-polarity legs of a sheared magnetic arcade into contact at a PIL to initiate runaway tether-cutting reconnection. This reconnection forms and/or grows a flux rope above the reconnection location, and this flux rope immediately starts erupting outward. As it does so, the region of the magnetic reconnection above the PIL and below the outward-moving flux rope continues to grow larger and move higher; this is the flare reconnection in the above description of the CSHKP model. Observational events have been observed and interpreted using this model (e.g. [Liu et al. 2012, 2013](#); [Chen et al. 2014](#); [Joshi et al. 2014](#); [Xue et al. 2017](#), and references cited therein).

Another eruption model, called “magnetic breakout” ([Antiochos et al. 1999](#)), assumes an initial quadrupolar magnetic configuration, where a flux rope erupts from the PIL of a “core” sheared magnetic arcade embedded in an opposite-direction larger arcade. The model argues that reconnection at the magnetic null above the sheared arcade initiates the eruption of the sheared arcade; the strongest flare reconnection then occurs at a current sheet at, again, the same location as in the CSHKP model: above the PIL of the sheared core field

and below the erupting flux rope. Various observational features of this model have been observed in observational events (e.g. [Aulanier et al. 2000](#); [Sterling & Moore 2001b, 2004](#); [Aurass et al. 2013](#); [Chen et al. 2016](#), and references cited therein).

Other ideas have also been put forth for the onset of the magnetic eruptions that make flares and CMEs, including the ideal magnetohydrodynamic instabilities known as the “kink instability” ([Török et al. 2004](#); [Török & Kliem 2005](#)) and the “torus instability” ([Kliem & Török 2006](#)). Also, recently there have been other proposed 3D models based on both observations and simulations, such as the “standard model in three dimension” ([Aulanier et al. 2012](#); [Janvier et al. 2014](#); [Li & Zhang 2015](#); [Gou et al. 2016](#); [Dudík et al. 2016](#)). This MHD model includes the eruption of a torus-unstable magnetic flux rope via the torus instability, and reconnection at a current sheet that forms underneath the erupting flux rope. The current layers are regions of high magnetic field gradient, known as “quasi-separatrix layers (QSLs; [Priest & Démoulin 1995](#); [Démoulin et al. 1996](#)). The slipping-reconnection concept has also been proposed as a mechanism to initiate solar flares/eruptions ([Aulanier et al. 2006](#); [Dudík et al. 2014](#)). Moreover, the slipping reconnection itself has been proposed to be the tether-cutting mechanism ([Dudík et al. 2016](#)). Models such as the “slipping reconnection” model (e.g. [Dudík et al. 2016](#)) or the “Standard solar flare model in 3D,” (e.g. [Aulanier et al. 2012](#)) incorporate the 2D CSHKP model in a 3D view.

The field configurations and initiation of three-ribbon flares, with two parallel ribbons and a third circular ribbon occurring in the same flux-rope-eruption episode, have not been investigated extensively. In one recent such study, [Joshi et al. \(2015\)](#) discussed the magnetic topology and triggering of such a three-ribbon flare; they suggested a possible scenario for the event they observed, and recently [Carley et al. \(2016\)](#) presented support for that scenario based on solar radio data. In the present work, we present observations of a different example of a similar three-ribbon-flare eruption. It is an ejective eruption of a sigmoid flux rope, and occurred on 2014 December 18 in a large-scale fan-spine type magnetic configuration. Our main aim in this study is to determine how the eruption was initiated and how it produced the three-ribbon flare. We will also discuss similar eruptions that occur on a much smaller size scale in the form of coronal jets; recently it has been recognized that many such jets result from small-scale “minifilament” eruptions, which appear to be scaled-down versions of larger sheared-core arcade eruptions that make flares and CMEs ([Sterling et al. 2015](#)). The magnetic geometry we describe for our large-scale three-ribbon flare is also present in the jets produced by minifilament eruptions, and those jets also have a similar pattern of three flare ribbons.

We construct this paper in the following sections. Section 2 explains about the observational data sets used. Source region location information and overlying magnetic topol-

ogy are discussed in Section 3. Multiwavelength analysis are presented in Section 4, with GOES and RHESSI flux temporal evolution (Section 4.1), parallel ribbon formation dynamics (Section 4.2), circular ribbon formation dynamics (Section 4.3), discussion about ribbons formation timings (Section 4.4), and associated CME (Section 4.5). A comparison with the coronal jet topology is presented in Section 5. The main results and their discussions are presented in Section 6.

## 2. Instrumentation

We use data from several space-based instruments: *SDO*/AIA and HMI, *GOES* and *RHESSI*. The Atmospheric Imaging Assembly (AIA; [Lemen et al. 2012](#)) is an instrument on board the *Solar Dynamics Observatory* (*SDO*) that observes the Sun in visible, ultraviolet (UV), and extreme ultraviolet (EUV) wavelengths. For the present work we have examined AIA observations at all available EUV channels: 304, 131, 171, 193, 211, 335, and 94 Å, and also in UV at 1600 and 1700 Å, and in visible light at 4500 Å. AIA has temporal cadences of 12 s for EUV and 24 s for UV, and pixel size of 0.6". The Helioseismic and Magnetic Imager (HMI; [Schou et al. 2012](#)) is another instrument on board *SDO*. It provides line-of-sight magnetic field maps of the whole face of the Sun with a temporal cadence of 45 s and with pixel size of 0.5". For observing the X-ray-coronal and footpoint sources during the flare we use data from the *Reuven Ramaty High-Energy Solar Spectroscopic Imager* (*RHESSI*; [Lin et al. 2002](#)), where we used the PIXON algorithm for image reconstruction with an integration time of around 20 s.

## 3. Source Region Location, Morphology and Magnetic Field Structure

Figure 1 is a montage of *SDO*/AIA 304, 171 and 4500 Å images showing an overview of the active region (AR) that was the source of the event, NOAA AR 12241. The background image is a *SDO*/AIA 304 Å full disk image from 21:30:07 UT on 2014 December 18 (Figure 1(a)). The black box in Figure 1(a) shows the location of AR 12241, with closeup images in *SDO*/AIA 4500 Å and 171 Å respectively in Figures 1(b) and 1(c). These images show that AR 12241 is located near disk center, and the *SDO*/AIA 4500 Å image shows that the AR consists a group of several sunspots, with one leading sunspot and three relatively small following sunspots (arrows in Figure 1(b)). The magnetic class of the active region was  $\alpha\beta\gamma$  on 2014 December 18.

Figure 2 shows the line-of-sight photospheric magnetogram corresponding to the area

shown in the black box of Figure 1(a). This magnetogram is from 21:30:24 UT on 2014 December 18, and shows that the active region is bipolar with much of its positive-polarity magnetic flux in the large leading sunspot and much of its negative flux in the three following sunspots, and has a long PIL between its positive and negative flux domains. Also marked in the figure is an extensive region of negative polarity that surrounds the positive flux domain region. This photospheric magnetic distribution suggests that there should be a large-scale fan-spine type configuration with a shell of open or far-reaching field outside of the AR that is rooted in the surrounding negative-polarity region and extending far above and away from the AR; thus the AR would be inside of this shell, and so will call this shell the “outer shell.” There is also a portion of the fan field inside of that outer shell, i.e. an “inner shell,” which is an anemone-shaped ring of field loops having one foot in the positive flux domain and the other foot in the surrounding negative domain. As we will see shortly, the strip along the PIL in the red box is the site of formation of a flux rope that erupts; it is that eruption and its interaction with the shells of the fan that produce the three flare ribbons.

In Figure 3 we confirm the existence of a huge fan-spine structure using a potential-field source-surface (PFSS, Schrijver & De Rosa 2003) extrapolation in the neighborhood of the AR, where we accessed the PFSS package with the Interactive Data Language (IDL) using the Solar Software (SSW) package (Freeland & Handy 1998). Figure 3(a) shows a full disk magnetogram from 18:03:28 UT on 2014 December 18 with the extrapolated potential field lines overplotted, and Figure 3(b) shows a closeup of the active region corresponding to the region of the black box in Figure 3(a). The closed field lines (shown in white) are the field lines of the inner fan dome, while the open field lines (pink) represent the field lines of the outer shell of the fan dome. The inner (closed) and outer (open) fan-dome fields are expected to be separated by a separatrix layer in 3D. As we will show below, this configuration is well-matched with the *SDO*/AIA observations (see Sections 3, and 5). Later (Section 5), we will show that this configuration is similar to a typical coronal-jet-base field configuration with an inferred fan-dome field topology in the corona (Sterling et al. 2015).

## 4. Multiwavelength Analysis of the Ejective Eruption and Flare Dynamics

### 4.1. *GOES* and *RHESSI* X-ray Intensity Profiles

Figure 4 shows the *Geostationary Operational Environmental Satellite* (*GOES*) and *RHESSI* X-ray time profiles of the flare. The black solid and dashed curves are the *GOES* X-ray profiles for 1–8 Å and 0.5–4 Å respectively, and the *RHESSI* X-ray profiles at 3–6 keV (pink), 6–12 keV (red), 12–25 keV (green), and 25–50 (blue) keV are overplotted. This flare was class M6.9 on the *GOES* X-ray scale. From the *GOES* profiles we see that the

flare started at  $\sim 21:41$  UT and peaked at  $\sim 21:58$  UT, and had an extended decay phase that continues until  $\sim 02:00$  UT on 2014 December 19. The overall variation of the *RHESSI* X-ray profiles matches with that of the *GOES* profiles.

#### 4.2. Two-Ribbon Component: Standard Reconnection and Parallel Ribbons Formation

The event consists of two different aspects, or “components.” One component is a standard sheared-core-arcade flux-rope eruption, including the standard CSHKP-type flare reconnection and parallel ribbon formation discussed above, all occurring inside of (and perhaps initiated independently of) the large-scale fan-spine structure. Figures 5((a)–(e)) present a sequence of *SDO/AIA* 131 Å images during the time of dynamic evolution of the flux rope, including its formation, eruption, and triggering of CSHKP-type flare reconnection. The first indication of the flare onset in these images seems to be at  $\sim 21:30$  UT, with a compact brightening at the location of the red circle in Figure 5(a). This brightening may be due to tether-cutting reconnection occurring between low-lying sheared arcade loops with the footpoints of their legs anchored in opposite-polarity footpoint regions. We can identify candidates for these loops as dark arch-like structures on the eastern and western sides of the red circle; they are shown as red- and blue-dashed curves in Figure 5(a), and respectively labeled “WA” and “EA” for western and eastern loops of a highly-sheared arcade. We further examine the anchoring of the arcade loops as well as the location of the compact brightening by comparing the *AIA* 131 Å images with *SDO/HMI* photospheric magnetogram, by overplotting WA and EA of Figure 5(a) onto the magnetogram of Figure 5(f). This shows that the far ends of the WA and EA arcade loops are anchored in negative and positive polarity regions, respectively. The location of the initial compact brightening region (red circles in Figs. 5(a) and 5(f)) is near the junction of the two arcades.

Inspection of the *SDO/HMI* photospheric magnetic field movie (see animation accompanying Figure 5) of the area shows rapid evolution, with continuous flux cancellation and shearing motions; in particular, the red-circled area in Figure 5(f) shows cancelation occurring in the hours prior to the onset of flaring, with an episode of cancelation between the positive-polarity patch with adjacent negative-polarity flux starting at about 20:15 UT. This rapid flux cancelation is a strong candidate for driving pre-eruption tether-cutting reconnection that could build a pre-eruption core flux rope. That is, this pre-eruption tether-cutting reconnection is apparently driven by flux cancelation resulting from evolutionary photospheric motions.

Soon after the initial brightening, we observe the formation and appearance of long

thread-like structures over the flux-cancellation region (Figures 5(b)–(e)). These are perhaps best visible in 131 Å and 94 Å wavelengths, from about 21:35 UT (or even earlier in 94 Å), where they appear in emission; they are faintly visible in 193 Å images, but more difficult to see or invisible at this early stage (when they are low down in the core region) in other wavelengths. These newly-formed long structures are consistent with them being a component of the flux rope expected to result from tether-cutting reconnection below. Thus, similar to some other cases (e.g., Cheng et al. 2013; Sterling et al. 2014), the erupting flux rope tends to be visible in (some) hotter AIA EUV channels, but faint or invisible in the cooler AIA channels.

In this case, although a cool-material filament is clearly visible along the PIL, there is no clear evidence that any of this filament material is ejected along with the hotter flux rope. (A strand of this filament is ejected from the west side of the filament at ~21:51 UT, but this is a secondary aspect of the flux-rope eruption, in the sense that it occurs well after the two parallel ribbons start to separate; we do not consider here whether this strand ejection is connected to the null-point reconnection (Section 4.3) that begins at about the same time.) Ribbon-like brightenings from the eruption start parallel to the filament along either side of the filament; these features are perhaps most apparent in the 304 Å images (not included here), but they can also be seen in the movie accompanying Figure 5(a). This suggests that the suspected tether-cutting reconnection occurred among fields overlying the filament (e.g., Moore & Sterling 2007), and therefore the flux-rope formed and was expelled from a location above the filament, leaving the filament inside the flare arcade.

In Figure 5(d) we trace the observed front of the newly-formed flux rope with a dotted black line, and in Figure 5(f)) we overplot that trace onto an *SDO*/HMI photospheric magnetogram. This shows that the eastward leg of the observed flux rope is anchored in a negative-polarity region, and the westward leg is anchored in a positive-polarity region. This configuration supports that this observed outward-moving bright feature is indeed a flux rope that forms from runaway tether-cutting reconnection early in the eruption. (By “runaway tether cutting,” we mean a situation whereby the tether-cutting reconnection promotes further tether-cutting reconnection through a positive-feedback process for an extended period of time.) We also observe flare brightening along the PIL location below the erupting flux rope in all AIA EUV wavelengths as the flux rope moves outward (see Figures 5(d) and (e), and accompanying video). This flaring is expected as the legs of the arcade enveloping the erupting flux rope partake in the CSHKP-type reconnection.

Figure 6 shows the outward propagation of the flux rope in *SDO*/AIA 131 Å running-difference images, where we highlight the approximate front of the flux rope by the dashed red lines. We can gain insight into the temporal relation between the erupting flux rope, the

flare brightening, and the formation of the ribbons by comparing the height-time profile of the erupting flux rope’s leading edge with the *GOES* X-ray profiles (Figure 7).

The left panel of Figure 7 shows an *SDO/AIA* 131 Å image at 21:47:08 UT and the red dashed line along which the projected height of the erupting flux rope has been measured. The height-time profile is shown in the right panel of Figure 7. To determine the height-time data points, we tracked the leading edge of the erupting flux rope along the red dashed line in Figure 7(a), where the bottom-most point of the line is used as a reference point for the height measurements. To estimate the uncertainty in the height-time locations we repeated the same analysis three times, and the average of three values has been used as a final value of height-time measurements and the error bars are the  $1\sigma$  standard deviations resulting from those three repeated measurements. The speeds are calculated using linear fits to the different time intervals. The height-time profile reveals a two-phase evolution of the eruption: The first phase is during  $\sim 21:36$  UT to  $\sim 21:48$  UT, with an average speed of around  $48 \text{ km s}^{-1}$ , while the second phase is from  $\sim 21:48$  UT to  $\sim 21:55$  UT with a relatively higher average speed of around  $165 \text{ km s}^{-1}$ . The first and second phases are shown by the red and green fitted lines in Figure 7(b), respectively. We also overplotted the *GOES* 1-8 and 0.5-4 Å flux profiles with the height-time profile (shown by blue thick and dotted lines, respectively, in Figure 7(b)). It can be seen that the *GOES* X-ray flux enhancement is well matched with the height-time profile, suggesting that the flux rope’s upward motion is correlated with runaway tether-cutting reconnection underneath it. Two-step rise profiles (slow-rise and fast-rise phases) have commonly been seen for filament eruptions (e.g., Tandberg-Hanssen et al. 1980; Sterling & Moore 2005; McCauley et al. 2015), and in some cases accelerations in the filament trajectory have been also found to correspond to peaks in brightenings in *GOES* fluxes (e.g. Sterling et al. 2007, 2011). Thus, the flux-rope eruption behavior here is in agreement with those observations of erupting filaments (which are believed to be cool material riding on erupting flux ropes). The time-distance map of the eruption have also been shown in Figure 7(c).

The morphology of the parallel ribbons formation can be seen in the *SDO/AIA* 1600 Å observations (Figure 8). The initial ribbon brightening is observed over  $\sim 21:41$ — $\sim 21:42$  UT (Figure 8(a)). Early in the evolution of the flux rope, e.g. at about 21:47 UT (Figure 8(b)), we see multiple ribbons, broadly consistent with the four-ribbon configuration expected during the earliest stages of the tether-cutting scenario (see top-right panel of Fig. 1 in Moore et al. 2001). Later (e.g., 22:10 UT), these ribbons evolve into the standard parallel ribbons (see Figure 10(d)) along both sides of the PIL; the overall dynamics can be seen in the *SDO/AIA* 1600 Å movie (see animation accompanying Figure 10). Contours of the standard parallel ribbons observed in *SDO/AIA* 1600 Å are overplotted on line-of-sight HMI magnetogram in Figure 8(d), showing that the northern and southern parallel ribbons are located in negative

and positive polarity regions, respectively. The ribbons extend in the east-west direction and move apart in the north-south direction as the flux rope moves outward. Moreover, we also observed RHESSI 25–50 keV X-ray source on one of the two ribbons (see green contours in Figure 8(c)). These observations are consistent with the standard flare model, with runaway tether-cutting reconnection occurring below the erupting flux rope and with charged particles accelerated at the reconnection site and flowing downward along the magnetic field lines and striking the lower chromosphere to emit hard X-rays and heat the flare ribbons.

Figure 9 presents a schematic based on the observations in the various AIA EUV and 1600 Å channels and these discussions. We emphasize that all of these early-stage dynamics (erupting flux rope and two-ribbon flare) are occurring inside of the northeastern lobe of the huge fan-dome magnetic-field configuration (see red box in Figure 2).

### 4.3. Circular-Ribbon Component: Null point Reconnection and Circular Ribbon Formation

This component of the eruption is a consequence of the null-point reconnection, which results in the circular ribbon. It occurs because of the interaction of the erupting flux rope and the arcade containing it (where that arcade is the northeast side of the inner fan field prior to its eruption) described in Section 4.2 with the null of the fan-spine magnetic structure. The formation and dynamics of the circular ribbon can be understood by analyzing the *SDO/AIA* observations in different wavelengths (Figures 10 and 11).

Figure 10 shows a sequence of selected *SDO/AIA* 1600 Å images over ~21:53 UT to ~22:10 UT. The first appearance of the circular ribbon is between 21:52 UT and 21:53 UT, starting near the eastern end of the northern parallel ribbon (Figure 10(a)). The brightening in the circular ribbon then moves sequentially in a counterclockwise direction, first to the east and then to the south and then the west. The brightness reaches the far-southern extreme, opposite the parallel ribbons, at around ~21:55 UT, with a quasi-circular ribbon visible at around ~22:00 UT (Figure 10(c)). The brightness then continues moving further west, forming a near-circle at around ~22:10 UT (Figure 10(d)). This circular ribbon was visible in all of the *SDO/AIA* channels; Figures 11(a)–(e) respectively show the circular ribbon in *SDO/AIA* 171, 193, 131, 211, and 304 Å wavelengths. Figure 11(f) shows the circular ribbon overlaid onto an *SDO/HMI* line-of-sight photospheric magnetogram, with the ribbon in *SDO/AIA* 304 and 1600 Å displayed in green and red contours, respectively. This shows that the circular ribbon is situated in a negative-polarity region.

The RHESSI X-ray sources have also been observed during this phase in the region

between the parallel ribbons (see Figures 8(a)–(c)). This suggests that the standard reconnection underneath the erupting flux rope remains ongoing.

The null-point reconnection also heats a ring of new inner fan loops that are visible in hotter AIA channels. Figure 12 shows examples of these structures in *SDO*/AIA 335 and 94 Å images. Evidently, the erupting flux rope drives its enveloping arcade to reconnect at the null point in the higher corona, heating this circular ribbon. Figure 14 shows a schematic for this interpretation, and will be discussed further in Section 5.

#### 4.4. Ribbon Timings

In reconnection-initiated eruption-onset models, there are (at least) two different mechanisms by which reconnection can initiate the eruption of a flux rope: In the first case, the release of tension force below the flux rope initiates and grows the eruption; this is the runaway tether-cutting idea (Moore et al. 2001). As we have seen above (Section 2), it appears that such tether cutting produces the parallel flare ribbons under the erupting flux rope in our event. In the second mechanism, it is the removal of flux overlying the flux rope via reconnection at a fan null that initiates the flux rope’s eruption; this is the idea of the magnetic breakout mechanism (Antiochos et al. 1999). In our event, breakout reconnection evidently produces the circular ribbon at locations remote from the location from which the flux rope erupts.

As mentioned in Section 1, a third mechanism that may initiate eruptions is an ideal MHD instability not involving reconnection. We do not address this option directly here, in part because it is difficult to detect the earliest eruptive magnetic motion, since a distinct erupting filament that can often be used as a tracer of such early magnetic motion is not available in this event. We do however observe signatures of both tether cutting and breakout, and so here we address directly which of these two mechanisms shows the best evidence for initiating the eruption.

To decide which of these two scenarios best fits our event, we use the relative timing of the onset of the two different flare ribbons. If the parallel ribbons in the immediate vicinity of the flux rope brightened prior to the onset of brightening of the remote circular ribbon, that would be an indication that tether cutting precedes breakout. Should the order be reversed, that is if the circular ribbon started prior to the parallel ribbons, this would indicate that breakout precedes tether cutting. At least several previous attempts to address this question of tether cutting or breakout based on relative timing of two-ribbon flare brightening and remote brightening have been inconclusive, due to insufficient cadence of the observations

for the features being studied (e.g., [Moore & Sterling 2006](#)).

*SDO/AIA* 1600 Å images show that the parallel ribbons began no later than 21:38 UT, and they were essentially fully developed by ~21:50 UT. The circular ribbon on the other hand did not start until ~21:52 UT, and was not fully developed prior to ~21:55 UT. That is, the null-point reconnection began about 12 min later than the flux rope started to erupt in step with runaway tether-cutting reconnection and flare heating below (see [Figure 7\(b\)](#)). Therefore, in this case, the evidence unambiguously supports that the runaway tether-cutting reconnection under the rising flux rope preceded the breakout reconnection at the null point. Hence, in our case we conclude that the tether-cutting reconnection is more probable than breakout for the initiation of flux-rope eruption (see [Figure 5](#) and accompanying animation).

#### 4.5. Accompanying CME

This eruption is ejective in that it is accompanied by a CME. [Figure 13](#) shows a SOHO/LASCO white light coronagraph image of the CME at 01:04:42 UT on 2014 December 19. Unfortunately, due to a data gap, only a few images are available and so the CME was not observed at full cadence. This image shows that the CME accompanying the eruption was a halo CME, with the outer approximately-circular leading edge of the CME visible in this image.

### 5. Schematic and Comparison with Coronal Jet Topology

In our interpretation, this flux rope eruption and accompanying three-ribbon flare followed the two-component process outlined in [Sections 4.2 and 4.3](#). The schematic of [Figure 9](#), discussed above, describes the onset of the two-ribbon component. The schematic in [Figure 14](#) describes the overall evolution of the event, including the circular-ribbon-component null-point reconnection.

[Figures 14\(a\) and \(b\)](#) show the situation as the flux rope formed in the two-ribbon component of the event erupts outward from the surface. This flux-rope eruption occurs inside the smaller (i.e. more compact) lobe of the inner fan dome. Because we have learned that the two-ribbon component of the eruption precedes the circular-ribbon component, we infer that the circular-ribbon component of the event starts when the erupting flux rope induces reconnection of its arcade envelope at the null point between the closed (inner) and far-reaching (outer) portions of the fan structure. The null-point reconnection results in the circular ribbon when particles from the null-point reconnection travel along the new dome

field lines and impinge upon the chromosphere, heating that plasma to create the circular flare ribbon (Figure 14(c)). The circular ribbon structure can be seen clearly in several wavelength channels (Figures 10 and 11).

Several additional factors support our interpretation outlined in Figure 14: (1) the existence of null-point-like structure in the PFSS extrapolation; (2) the observation that the eruption of the flux rope is directed towards the null point; (3) the formation of the circular ribbon; and (4) the observed RHESSI X-ray sources below the erupting flux rope, which is consistent with the geometry of Figure 14. Thus the erupting flux rope plays a key role in driving both the standard flare reconnection (e.g., Liu et al. 2007) that results in the parallel ribbons, and the null-point breakout reconnection (e.g., Sun et al. 2013; Joshi et al. 2015) that results in the circular ribbon.

The schematic in Figure 14 for our event is essentially the same as the schematic in Sterling et al. (2015) for X-ray jets in polar coronal holes (and similar schematics for active region coronal jets in Sterling et al. 2016, 2017). The field configuration we observe for the large-scale three-ribbon event studied here has a base size of  $\sim 10^5$  km, as determined by the approximate diameter of the circular ribbon. For the coronal jets, the same configuration occurs on a substantially smaller size scale, with a base size of  $\sim 10^4$  km.

Other than size scale, the eruption in our event has two main differences from the jet eruptions of Sterling et al. (2015). First, the erupting flux rope in our event, as pointed out in Section 4.2, carried no trackable dark filament of cool plasma, whereas the erupting flux rope in each of the jets studied by Sterling et al. (2015) did carry a trackable minifilament of cool plasma. Second, the erupting sheared-core arcade with the erupting flux rope in its core in our event blows out into the high corona and solar wind as a CME (that is, in this case most of the erupting arcade is not opened by the breakout reconnection), whereas in the coronal jets of Sterling et al. (2015) that are blowout jets, all of the blown-out arcade, including its minifilament-carrying core, is opened by the null-point reconnection and becomes part of the spire of the jet.

Figure 14 shows a variation of the jet schematic given in Sterling et al. (2016) where the cool minifilament, which would reside inside of the curled field lines on the left-hand-side bipole in panel (a), is omitted; thus, in this case the curled field lines indicate a minifilament-flux rope field that does not carry cool material. This is a better match than the schematic in Sterling et al. (2016) for the situation studied here with the large-scale eruption that does not include an obvious erupting cool filament. Even in the case of coronal jets though, even without the minifilament the minifilament-flux rope field could erupt, just as the large-scale event studied here had an erupting flux rope that did not carry a filament. Such minifilament flux ropes without cool minifilament material may erupt to cause jets in some

cases (Sterling et al. 2017).

In Figure 14(b), reconnection is occurring beneath the erupting minifilament field, producing a brightening at the jet’s base (jet-base bright point, or JBP); this corresponds to the two-ribbon flare that we observe in the large-scale event here. Figure 14(c) shows the arcade envelope of the erupting minifilament during reconnection at the null, and this makes new hot loops on top of the larger bipole. The jet spire initially forms at the location of the null, and it can spread horizontally away from the JBP depending on the subsequent evolution of the erupting flux rope.

Comparing this jet picture with the large-scale eruption studied here, the JBP located between locations A and B of Figure 14(c) corresponds to the two-ribbon flare of Figure 9, and the large loop between locations B and C of Figure 14(c) corresponds to the illuminated inner fan dome. Comparing the jet schematics with the large-scale eruption in Figures 12, 14(c), and 14(d) shows well how the two circumstances are analogous: The JBP of jet is corresponds to the bright flare loops on the north side of the erupting region in Figures 12, and 14(c), and the new (red) field line over the larger lobe in Figure 14(c) corresponds to the heated and illuminated inner-fan loops of Figure 12.

Because Sterling et al. (2015) observed jets near the limb, remote flare brightenings in the form of a circular ribbon were not well situated for visual detection. Some studies of on-disk jets in active regions however observed such circular ribbons (e.g., Wang & Liu 2012, 2014; Jiang et al. 2015; Sterling et al. 2016; Zhang et al. 2016; Li et al. 2017). Similar circular ribbons are also apparent, but often with lower intensity, in quiet Sun jets (Panesar et al. 2016). Partial circles of illumination at the bases of surges have also been observed (e.g., Öhman 1972; Wang & Liu 2012; Sterling et al. 2016; Hong et al. 2017).

According to the schematic of Sterling et al. (2015) (Figure 2 of that paper), a variation of which is the Figure 14 schematic, the implication is that in jets the JBP-producing flare reconnection occurs prior to the null-point reconnection, which in Figure 14 does not occur until panel (c). Actually however, whether the JBP-producing reconnection or the null-point reconnection occurs first in jets is so far an unexplored question. Our work here in Section 4.4 indicates that, at least for the large-scale eruptions presented here, the flare reconnection precedes the null-point reconnection.

Regarding the longer-term evolution, in the case of the jet, the erupting minifilament-flux-rope field moves out in a columnated fashion to form the jet. Typically however the erupting minifilament flux rope completely reconnects with the surrounding open (or far-reaching) field, and thus tends to have a highly-columnated jet structure. In the large-scale eruption, the flux rope contains enough flux so that the reconnection with the surrounding

field does not consume much of the flux rope, and so the erupting arcade with the flux rope in it largely escapes intact to become the CME with a flux-rope core.

Therefore, the magnetic conditions resulting in the double-ribbon eruption of 2014 December 18 studied here happen across the wide range of size scales of solar eruptive events.

## 6. Discussion

We have presented a detailed analysis of an ejective eruption accompanying a *GOES* M6.9 class flare, using multi-wavelength data sets from *SDO/AIA*, *RHESSI* and *GOES*. The eruption produced three flare ribbons: two parallel ribbons that form according to the standard eruption/flare model as a flux rope forms and erupts, and a circular ribbon resulting from null-point reconnection between the arcade envelope of that erupting flux rope with a fan canopy of open field. The main results of the work are as follows:

1. The observations as well as the PFSS extrapolation calculations clearly show the existence of a large-scale fan-spine type magnetic configuration over and around the eruption region. The northeast side of the inner fan lobe contains a strong neutral line on its inside.
2. The whole event has two aspects, or components: The “two-ribbon” component starts along the strong neutral line of the closed inner fan dome, and produces a flux rope and flare with parallel flare ribbons in accordance with the standard model for eruptions. The “circular-ribbon” component occurs when the enveloping arcade of the erupting flux rope undergoes reconnection at the null point of the overlying fan; this results in formation of a quasi-circular flare ribbon at the locations where the newly-closed fan field is rooted in the lower atmosphere.
3. The erupting flux rope therefore drives the production of all three flare ribbons. Standard flare tether-cutting reconnection is responsible for the formation of the two parallel ribbons, while the null-point reconnection is responsible for the large-scale quasi-circular ribbon.
4. Leading to the eruption onset, flux cancelation occurs along the main PIL from which the flux rope erupts, and at the location where the initial flare brightenings (pre-flare brightenings) occur. This is consistent with tether cutting from evolutionary photospherically-driven flux cancelation at the PIL triggering the eruption, and with runaway tether-cutting reconnection initiating the eruption and growing the flux rope.

5. A timing analysis shows that in this event the parallel ribbons unambiguously brightened prior to the onset of brightening of the circular ribbon. This is consistent with runaway tether-cutting reconnection starting prior to the start of the null-point “break-out” reconnection at the fan-dome magnetic null.
6. The observed magnetic topology and overall morphology is consistent with this eruption being a large-scale version of the same processes occurring in coronal jets that occur according to the minifilament-eruption picture.

There have been previous observational studies of eruptions resulting in circular ribbons, based on magnetic configurations similar to that we study here: a fan dome with an erupting bipolar region inside it. These studies encompass both relatively-small-scale (Sun et al. 2013; Jiang et al. 2013), as well as relatively-large-scale (Joshi et al. 2015) eruptions. Joshi et al. (2015) investigated a configuration similar to that here in a different large-scale eruption. The observed results in this eruptive event confirms the earlier proposed scenario by Joshi et al. (2015) for a similar kind of eruption and multiple ribbons flare. These studies show that the eruptions inside of fan structures is a common occurrence on the Sun. Remote flare brightenings (analogous to the circular ribbons observed here) and transient fan-like-loop heating can also occur in somewhat different magnetic geometries, such as when the arcade envelope of an erupting flux rope rams into nearby coronal hole field (Sterling & Moore 2001a).

In addition to studies suggesting that a flux rope (or sigmoid) eruption from the base of the fan dome drives null-point reconnection, and hence produces the circular ribbon flare (Sun et al. 2013; Jiang et al. 2014; Joshi et al. 2015), other studies suggest that shearing motion of the feet of the closed fan field by photospheric flow may drive the reconnection at the null point (Vemareddy & Wiegmann 2014). In our case here though it is very clear that the eruption of flux rope drives the null-point reconnection (see Section 4.2).

Also however, the sequential circular-ribbon brightening from east to west (see Figure 10 and accompanying animations) may provide some evidence of slip-running type reconnection at the null point. Similar sequential ribbon brightening has previously been observed and discussed (Masson et al. 2009; Reid et al. 2012; Sun et al. 2013).

The eruption of flux ropes to produce both a set of standard-flare parallel ribbons and a circular ribbon has only recently started to be studied in detail; our study here provides another example of such an event. These studies, together with those of jets and other phenomena, are helping to put together a coherent picture of various solar eruptions. Observational studies such as these promise to provide important input for numerical simulations of eruptions in various magnetic geometries. More observational studies as well as simulations

are needed to refine the understanding of such events. Moreover, the study of events such as the one here occurring near solar-disk center will provide important inputs for improving space weather forecasting.

The authors thank referee for their comments and suggestions. We thank the *SDO/AIA*, *SDO/HMI*, *GOES*, *SOHO/LASCO* and *RHESSI* teams for providing their data for the present study. This work is supported by the BK21 plus program through the National Research Foundation (NRF) funded by the Ministry of Education of Korea. NCJ thanks the School of Space Research, Kyung Hee University for providing a Postdoctoral grant. A.C.S. and R.L.M. were supported by funding from the Heliophysics Division of NASA’s Science Mission Directorate through the Heliophysics Guest Investigators (HGI) Program.

## REFERENCES

- Antiochos, S. K., DeVore, C. R., & Klimchuk, J. A. 1999, *ApJ*, 510, 485
- Aulanier, G., DeLuca, E. E., Antiochos, S. K., McMullen, R. A., & Golub, L. 2000, *ApJ*, 540, 1126
- Aulanier, G., Janvier, M., & Schmieder, B. 2012, *A&A*, 543, A110
- Aulanier, G., Pariat, E., Démoulin, P., & DeVore, C. R. 2006, *Sol. Phys.*, 238, 347
- Aurass, H., Holman, G., Braune, S., Mann, G., & Zlobec, P. 2013, *A&A*, 555, A40
- Benz, A. O. 2008, *Living Reviews in Solar Physics*, 5, 1
- Carley, E. P., Vilmer, N., & Gallagher, P. T. 2016, *ArXiv e-prints*
- Carmichael, H. 1964, *NASA Special Publication*, 50, 451
- Chen, H., Zhang, J., Cheng, X., Ma, S., Yang, S., & Li, T. 2014, *ApJ*, 797, L15
- Chen, Y., et al. 2016, *ApJ*, 820, L37
- Cheng, X., Zhang, J., Ding, M. D., Olmedo, O., Sun, X. D., Guo, Y., & Liu, Y. 2013, *ApJ*, 769, L25
- Démoulin, P., Henoux, J. C., Priest, E. R., & Mandrini, C. H. 1996, *A&A*, 308, 643
- Dudík, J., Janvier, M., Aulanier, G., Del Zanna, G., Karlický, M., Mason, H. E., & Schmieder, B. 2014, *ApJ*, 784, 144

- Dudík, J., et al. 2016, *ApJ*, 823, 41
- Fletcher, L., & Hudson, H. 2001, *Sol. Phys.*, 204, 69
- Freeland, S. L., & Handy, B. N. 1998, *Sol. Phys.*, 182, 497
- Gou, T., Liu, R., Wang, Y., Liu, K., Zhuang, B., Chen, J., Zhang, Q., & Liu, J. 2016, *ApJ*, 821, L28
- Hirayama, T. 1974, *Sol. Phys.*, 34, 323
- Hong, J., Jiang, Y., Yang, J., Li, H., & Xu, Z. 2017, *ApJ*, 835, 35
- Janvier, M., Aulanier, G., Bommier, V., Schmieder, B., Démoulin, P., & Pariat, E. 2014, *ApJ*, 788, 60
- Janvier, M., Aulanier, G., & Démoulin, P. 2015, *Sol. Phys.*, 290, 3425
- Jiang, C., Feng, X., Wu, S. T., & Hu, Q. 2013, *ApJ*, 771, L30
- Jiang, C., Wu, S. T., Feng, X., & Hu, Q. 2014, *ApJ*, 780, 55
- Jiang, F., Zhang, J., & Yang, S. 2015, *PASJ*, 67, 78
- Joshi, N. C., Filippov, B., Schmieder, B., Magara, T., moon, Y.-J., & Uddin, W. 2016a, *ApJ*, 825, 123
- Joshi, N. C., Liu, C., Sun, X., Wang, H., Magara, T., & Moon, Y.-J. 2015, *ApJ*, 812, 50
- Joshi, N. C., Magara, T., & Inoue, S. 2014, *ApJ*, 795, 4
- Joshi, N. C., Schmieder, B., Magara, T., Guo, Y., & Aulanier, G. 2016b, *ApJ*, 820, 126
- Joshi, N. C., Srivastava, A. K., Filippov, B., Uddin, W., Kayshap, P., & Chandra, R. 2013, *ApJ*, 771, 65
- Kliem, B., & Török, T. 2006, *Physical Review Letters*, 96, 255002
- Kopp, R. A., & Pneuman, G. W. 1976, *Sol. Phys.*, 50, 85
- Lemen, J. R., et al. 2012, *Sol. Phys.*, 275, 17
- Li, H., Jiang, Y., Yang, J., Yang, B., Xu, Z., Hong, J., & Bi, Y. 2017, *ApJ*, 836, 235
- Li, T., & Zhang, J. 2015, *ApJ*, 804, L8

- Lin, R. P., et al. 2002, *Sol. Phys.*, 210, 3
- Liu, C., Deng, N., Lee, J., Wiegelmann, T., Moore, R. L., & Wang, H. 2013, *ApJ*, 778, L36
- Liu, C., et al. 2012, *ApJ*, 745, L4
- Liu, C., Lee, J., Yurchyshyn, V., Deng, N., Cho, K.-s., Karlický, M., & Wang, H. 2007, *ApJ*, 669, 1372
- Masson, S., Pariat, E., Aulanier, G., & Schrijver, C. J. 2009, *ApJ*, 700, 559
- McCauley, P. I., Su, Y. N., Schanche, N., Evans, K. E., Su, C., McKillp, S., & Reeves, K. K. 2015, *Sol. Phys.*, 290, 1703
- Moore, R. L., & Labonte, B. J. 1980, In: in *IAU Symp. 91, Solar and interplanetary dynamics; Proceedings of the Symposium, Cambridge, Mass., August 27-31, 1979. (A81-27626 11-92)*, 207
- Moore, R. L., & Sterling, A. 2006, In: *Geophysical Monograph Series - Volume 165 - Title: Solar Eruptions and Energetic Particles*, 43
- Moore, R. L., & Sterling, A. C. 2007, *ApJ*, 661, 543
- Moore, R. L., Sterling, A. C., Hudson, H. S., & Lemen, J. R. 2001, *ApJ*, 552, 833
- Öhman, Y. 1972, *Sol. Phys.*, 23, 134
- Panesar, N. K., Sterling, A. C., Moore, R. L., & Chakrapani, P. 2016, *ApJ*, 832, L7
- Pariat, E., Antiochos, S. K., & DeVore, C. R. 2009, *ApJ*, 691, 61
- Priest, E. R., & Démoulin, P. 1995, *J. Geophys. Res.*, 100, 23443
- Priest, E. R., & Forbes, T. G. 2002, *A&A Rev.*, 10, 313
- Reid, H. A. S., Vilmer, N., Aulanier, G., & Pariat, E. 2012, *A&A*, 547, A52
- Schmieder, B., Aulanier, G., & Vršnak, B. 2015, *Sol. Phys.*, 290, 3457
- Schou, J., et al. 2012, *Sol. Phys.*, 275, 229
- Schrijver, C. J., & De Rosa, M. L. 2003, *Sol. Phys.*, 212, 165
- Shibata, K. 1999, *Ap&SS*, 264, 129
- Shibata, K., & Magara, T. 2011, *Living Reviews in Solar Physics*, 8, 6

- Shibata, K., Masuda, S., Shimojo, M., Hara, H., Yokoyama, T., Tsuneta, S., Kosugi, T., & Ogawara, Y. 1995, *ApJ*, 451, L83
- Sterling, A. C., Harra, L. K., & Moore, R. L. 2007, *ApJ*, 669, 1359
- Sterling, A. C., & Moore, R. L. 2001a, *ApJ*, 560, 1045
- Sterling, A. C., & Moore, R. L. 2001b, *J. Geophys. Res.*, 106, 25227
- Sterling, A. C., & Moore, R. L. 2004, *ApJ*, 602, 1024
- Sterling, A. C., & Moore, R. L. 2005, *ApJ*, 630, 1148
- Sterling, A. C., Moore, R. L., Falconer, D. A., & Adams, M. 2015, *Nature*, 523, 437
- Sterling, A. C., Moore, R. L., Falconer, D. A., & Knox, J.-M. 2014, *ApJ*, 788, L20
- Sterling, A. C., Moore, R. L., Falconer, D. A., Panesar, N.-K., Akiyama, S., Yashiro, S., & Gopalswamy, N. 2016, *ApJ*, 821, 100
- Sterling, A. C., Moore, R. L., Falconer, D. A., Panesar, N.-K., & Martinez, F. 2017, *ApJ*, submitted
- Sterling, A. C., Moore, R. L., & Freeland, S. L. 2011, *ApJ*, 731, L3
- Sturrock, P. A. 1966, *Nature*, 211, 695
- Sturrock, P. A., Kaufman, P., Moore, R. L., & Smith, D. F. 1984, *Sol. Phys.*, 94, 341
- Su, Y., van Ballegooijen, A., Schmieder, B., Berlicki, A., Guo, Y., Golub, L., & Huang, G. 2009, *ApJ*, 704, 341
- Sun, X., Hoeksema, J. T., Liu, Y., Aulanier, G., Su, Y., Hannah, I. G., & Hock, R. A. 2013, *ApJ*, 778, 139
- Tandberg-Hanssen, E., Martin, S. F., & Hansen, R. T. 1980, *Sol. Phys.*, 65, 357
- Török, T., Aulanier, G., Schmieder, B., Reeves, K. K., & Golub, L. 2009, *ApJ*, 704, 485
- Török, T., & Kliem, B. 2005, *ApJ*, 630, L97
- Török, T., Kliem, B., & Titov, V. S. 2004, *A&A*, 413, L27
- Tsuneta, S., Masuda, S., Kosugi, T., & Sato, J. 1997, *ApJ*, 478, 787
- Vemareddy, P., & Wiegmann, T. 2014, *ApJ*, 792, 40

Wang, H., & Liu, C. 2012, ApJ, 760, 101

Wang, H., & Liu, C. 2014, ApJ, 781, L23

Xue, Z., Yan, X., Yang, L., Wang, J., & Zhao, L. 2017, ApJ, 840, L23

Zhang, Q. M., Li, D., Ning, N. J., Su, Y.-N., Ji, H. S., & Guo, Y. 2016, ApJ, 827, 27

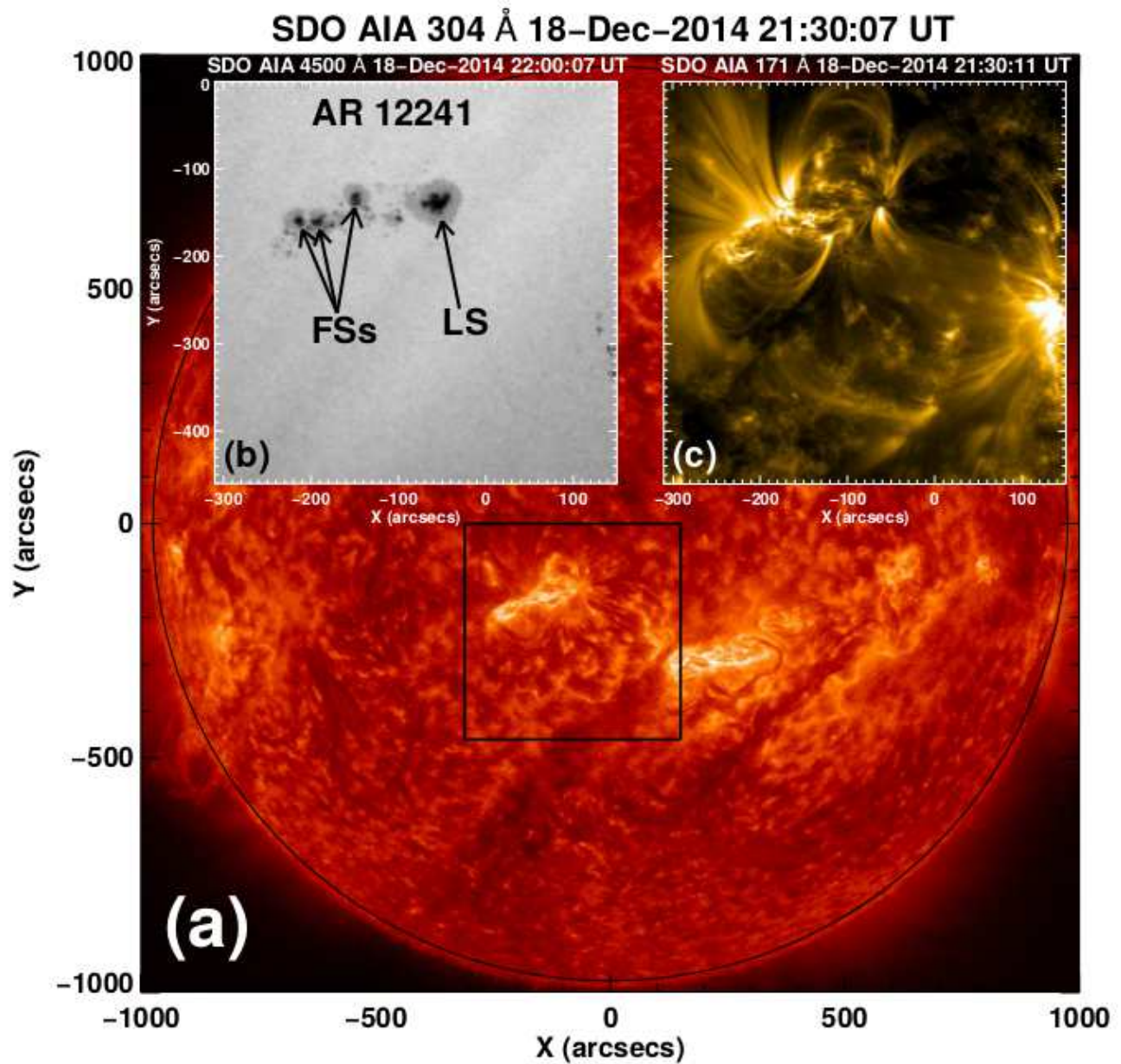


Fig. 1.— (a)(Background image) *SDO/AIA* 304 Å full disk image at 21:30:07 UT on 2014 December 18. The black box shows the active region location and the area of flare activity. Inserts are *SDO/AIA* 4500 Å (b) and 171 Å (c) zoomed images, corresponding to the black box shown in (a). The leading sunspot (LS) and following sunspots (FSs) are indicated in panel (b).

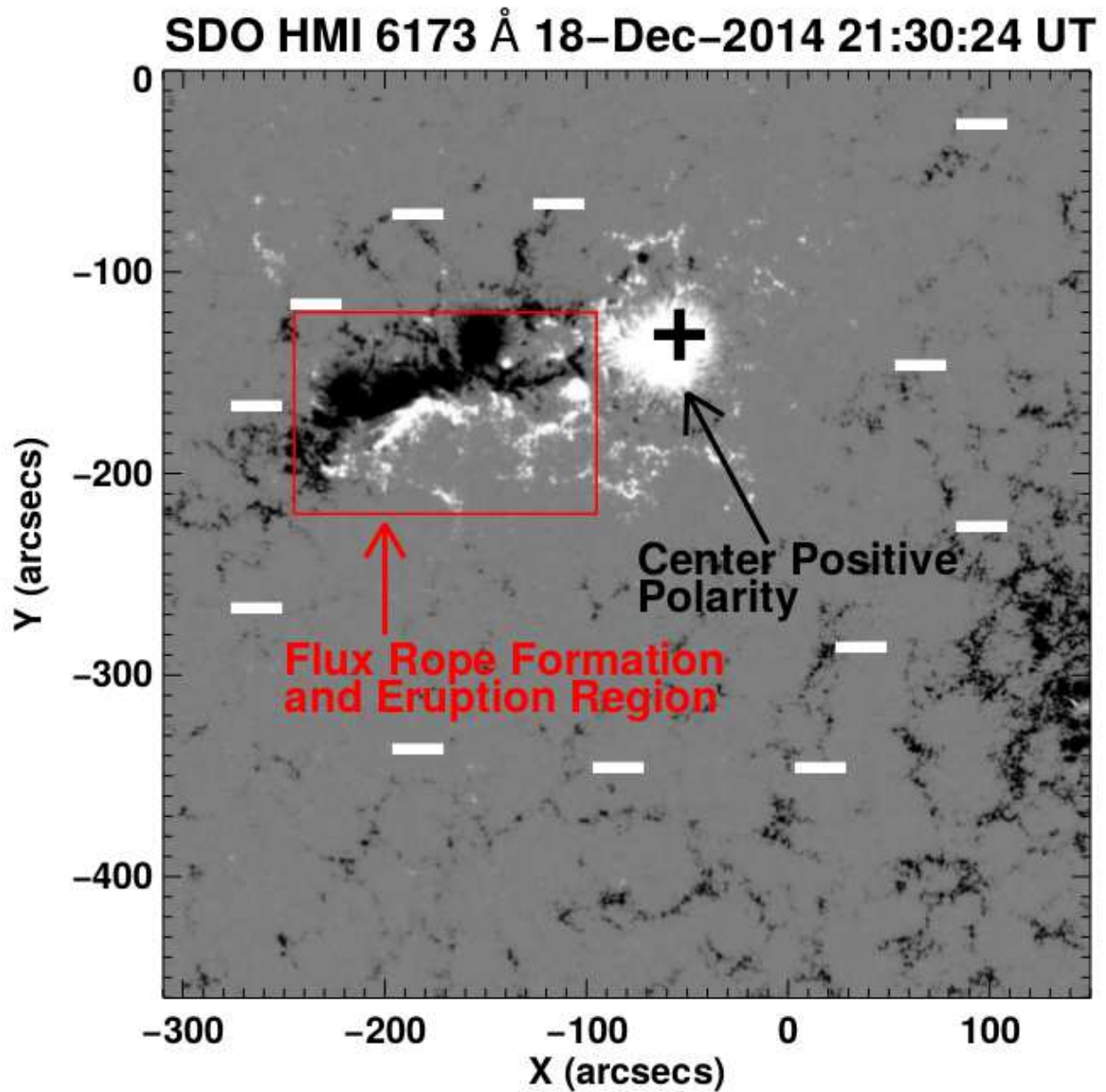


Fig. 2.— *SDO*/HMI line-of-sight photospheric magnetogram at 21:30:24 UT on 2014 December 18. The area of this image corresponds to the black box in Figure 1(a). The red box represents the site of flux-rope formation and eruption.

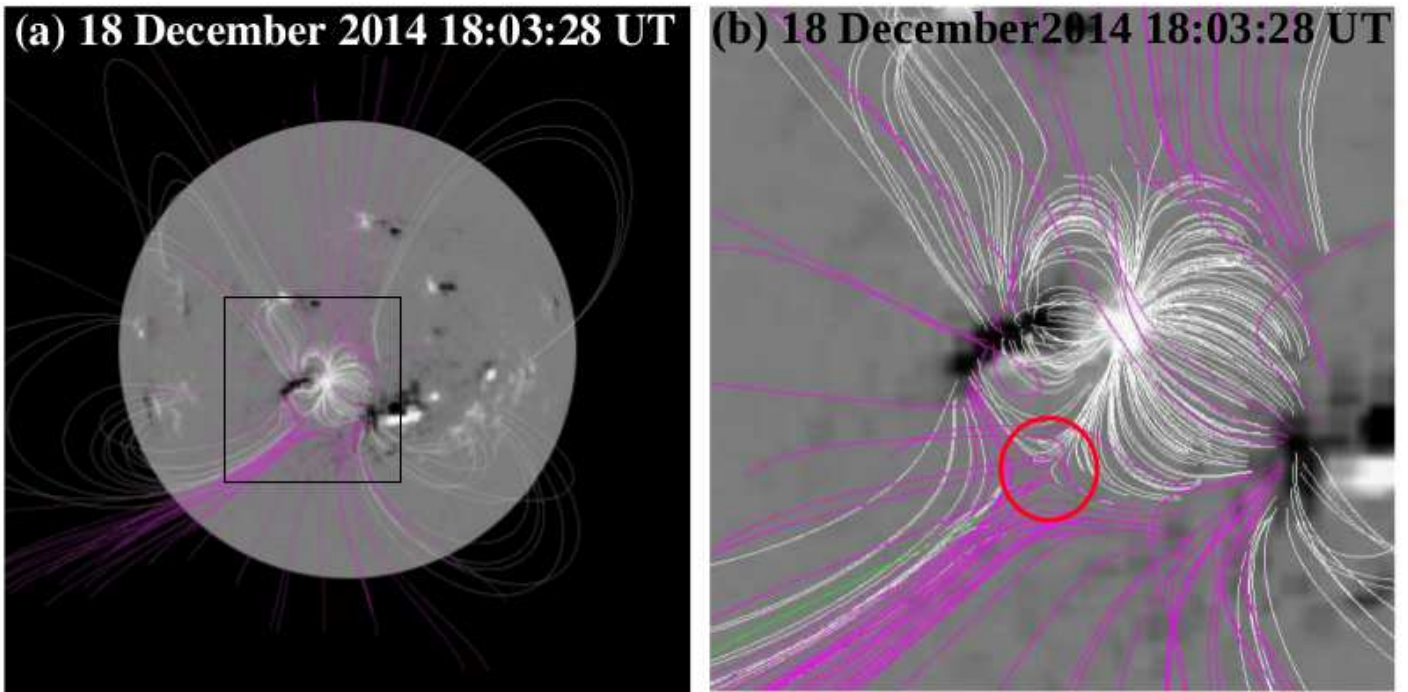


Fig. 3.— (a) PFSS magnetic field extrapolation showing a full disk view of the coronal magnetic field structure over the active region. (b) A zoomed view corresponding to the black box in (a). The white and pink lines represent closed and open field lines rooted in and around the active region, respectively. The magnetic null is inside the red circle in (b).

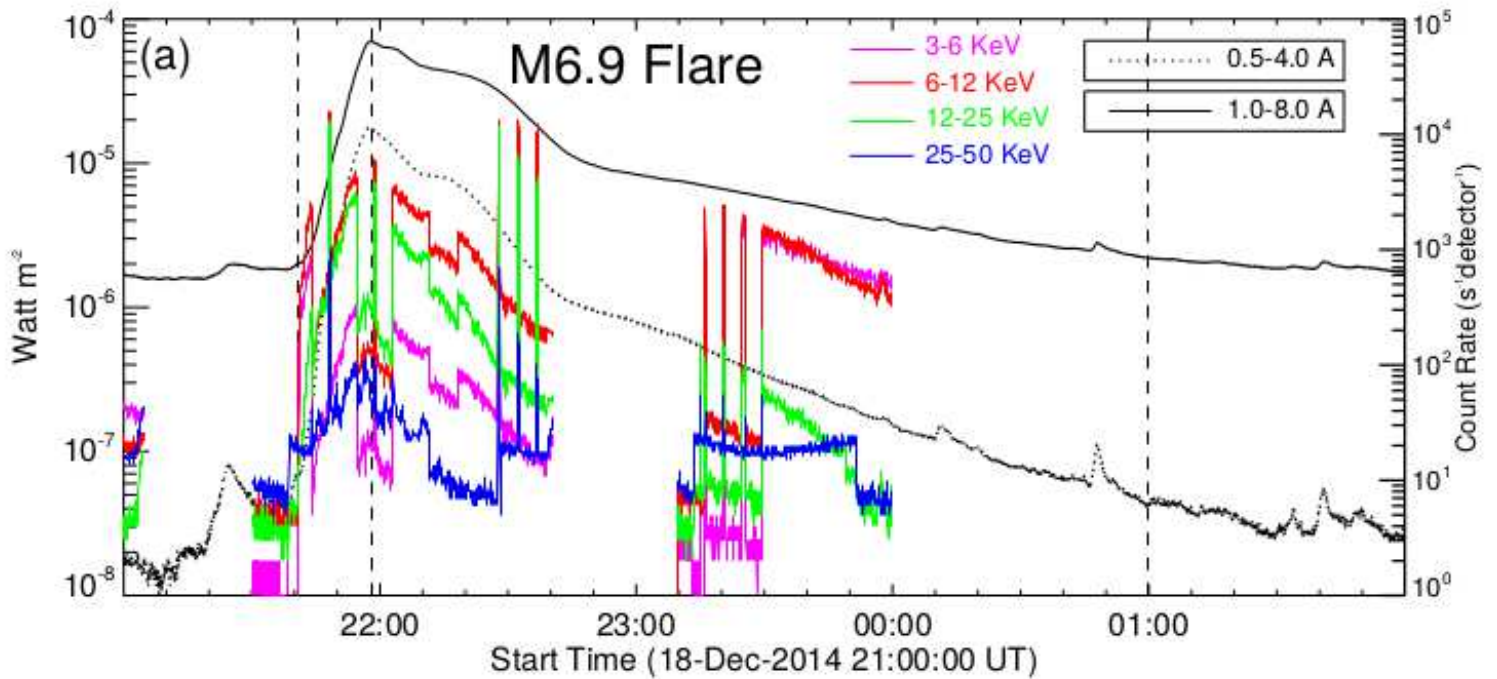


Fig. 4.— *GOES* and *RHESSI* X-ray flux time profiles from 21:00 UT on 2014 December 18 to 03:00 UT on 2014 December 19. The flare’s start ( $\sim 21:41$  UT), peak ( $\sim 21:58$  UT) and very late ( $\sim 1:00$  UT) times are indicated by the three dashed lines from left to right, respectively.

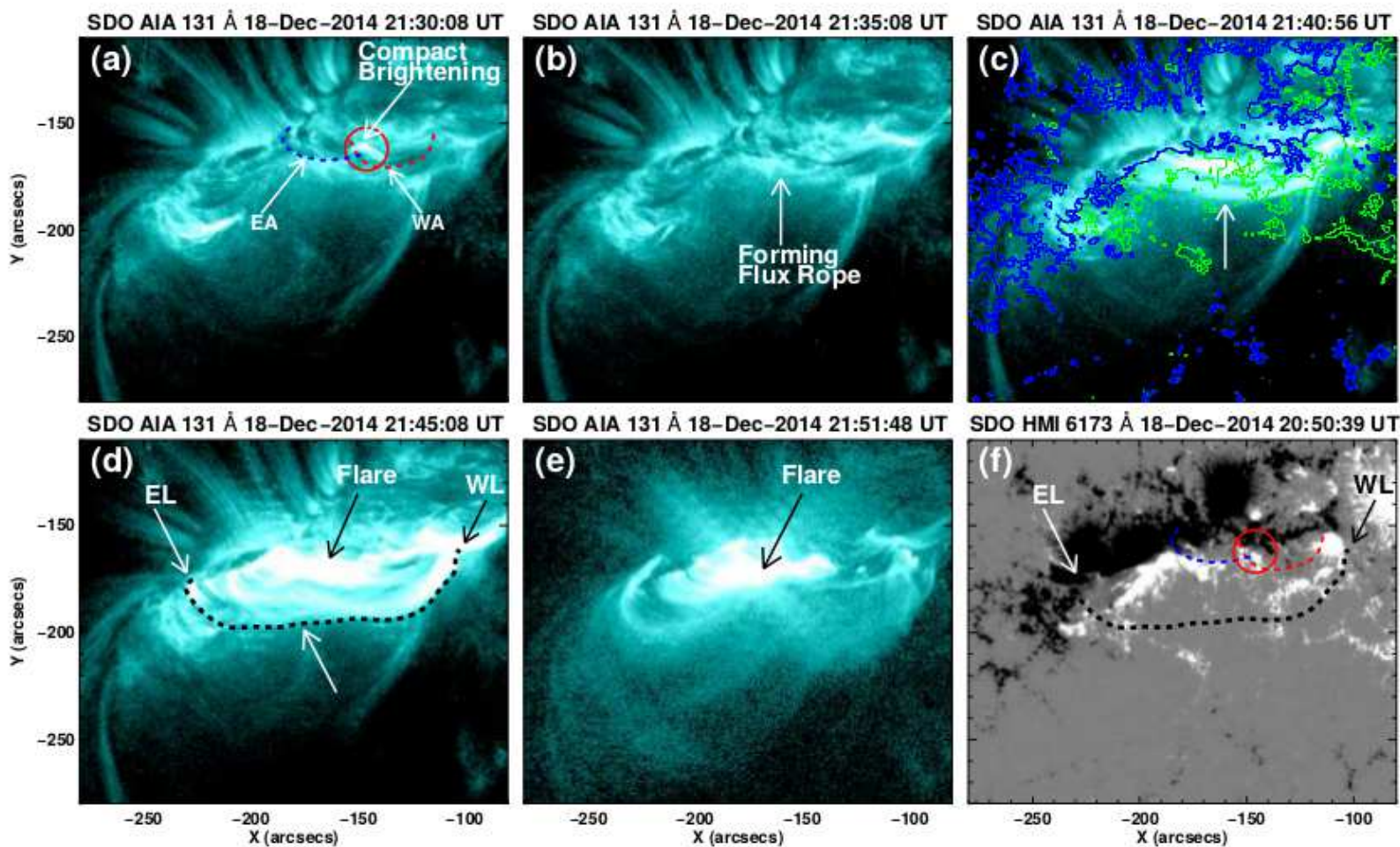


Fig. 5.— ((a)–(e)) *SDO/AIA* 131 Å images showing the evolution of the two-ribbon component of the eruptive event, with formation and eruption of the flux rope and standard flare reconnection over  $\sim 21:30$  UT to  $\sim 21:51$  UT on 2014 December 18. (f) *SDO/HMI* line-of-sight photospheric magnetogram at 20:50:39 UT on 2014 December 18. The dashed red and blue curved lines in panels (a) and (f) represent the eastern (EA) and western (WA) loops of the pre-eruption sheared arcade, respectively. The red circle in panels (a) and (f) represents the location of an initial compact brightening region in (a). The curved dotted black line in panels (d) and (f) show the front part of the moving flux rope at 21:45:08 UT. In panel (c) the blue and green contours show the photospheric magnetic field contours for negative- and positive-polarity field, respectively, with contour levels of  $\pm 40$ ,  $\pm 50$ , and  $\pm 100$  Gauss.

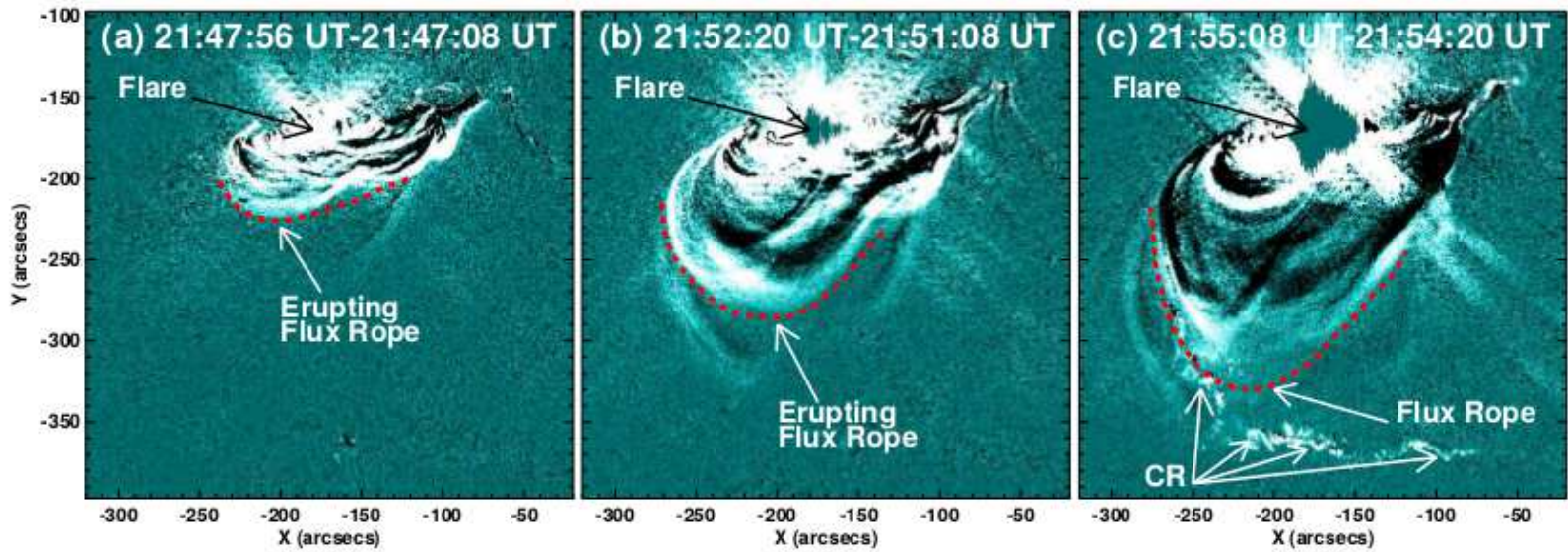


Fig. 6.— *SDO/AIA* 131 Å running-difference images showing the erupting flux rope, the two-ribbon-flare ribbons, and the circular ribbon (CR). The red dashed line shows the leading edge of the erupting flux rope.

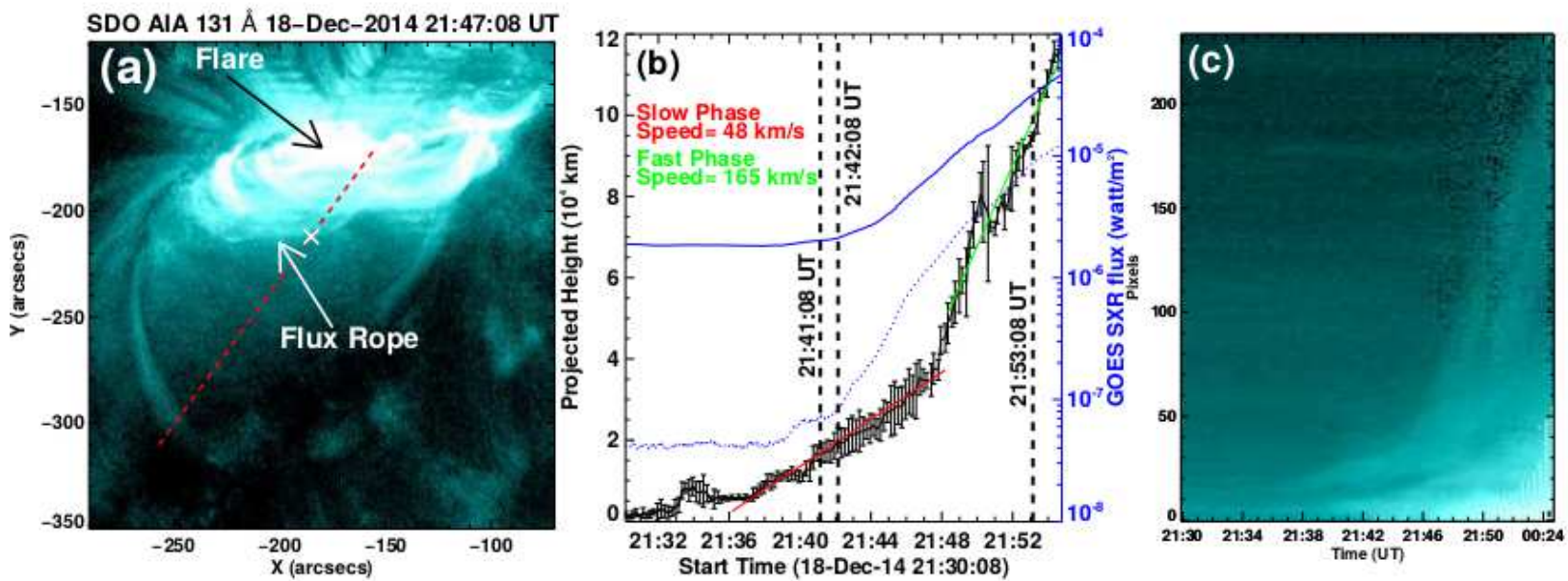


Fig. 7.— Left panel: *SDO/AIA* 131 Å image at 21:47:08 UT on 2014 December 18. The red dashed line is the path along which the height measurements and distance-time map are made. Middle panel: height-time profile of the leading edge of the erupting flux rope. The *GOES* X-ray profiles at 1–8 (blue solid curve) and 0.5–4 (blue dotted curve) Å channels are also overplotted. The speeds are from the red and green linear fits to the height-time data points. The "X" in panel (a) represents the location where the flux rope is being measured at the time of this image. The vertical dashed lines from left to right represent the start time of flare, first appearance of parallel ribbons and first appearance of circular ribbon. Right panel: Time-distance map of the eruption long the red dashed line of (a).

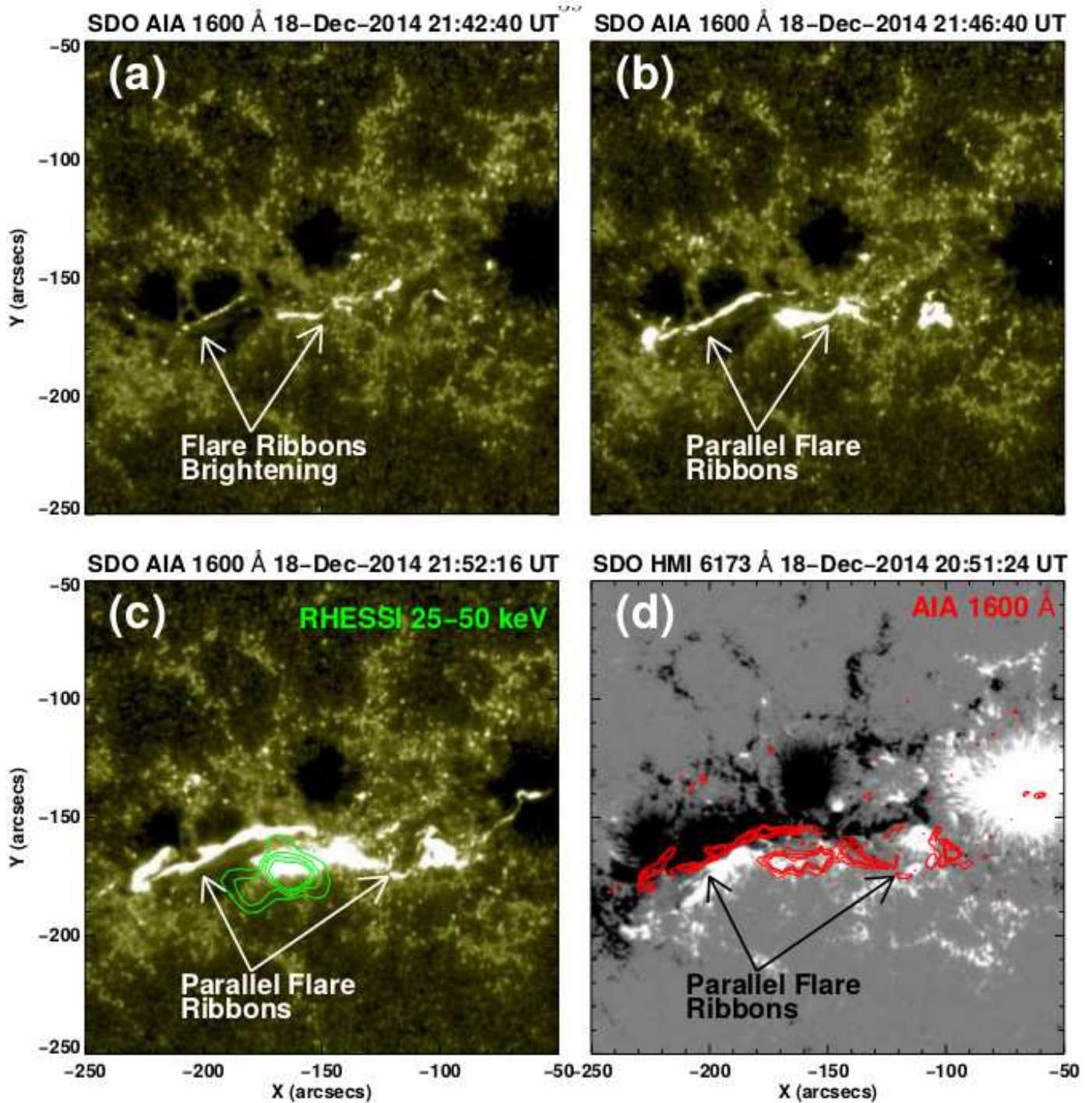


Fig. 8.— ((a)–(c)) *SDO/AIA* 1600 Å image sequence, showing the formation of standard parallel ribbons during the first stage of the eruption event. (d) *SDO/HMI* line-of-sight photospheric magnetogram at 20:51:24 UT. The overplotted red contours are of *SDO/AIA* 1600 Å intensity, showing the parallel ribbons at 21:52:16 UT (the time of panel (c)). The contour levels are 5%, 10%, 20%, and 30% of the peak intensity. The green contours in panel (c) image the *RHESSI* X-ray intensity in the energy range 25–50 keV, generated with the PIXON algorithm. The contours levels are 20%, 30%, 40%, and 50% of the peak intensity, and the integration time is 20 s.

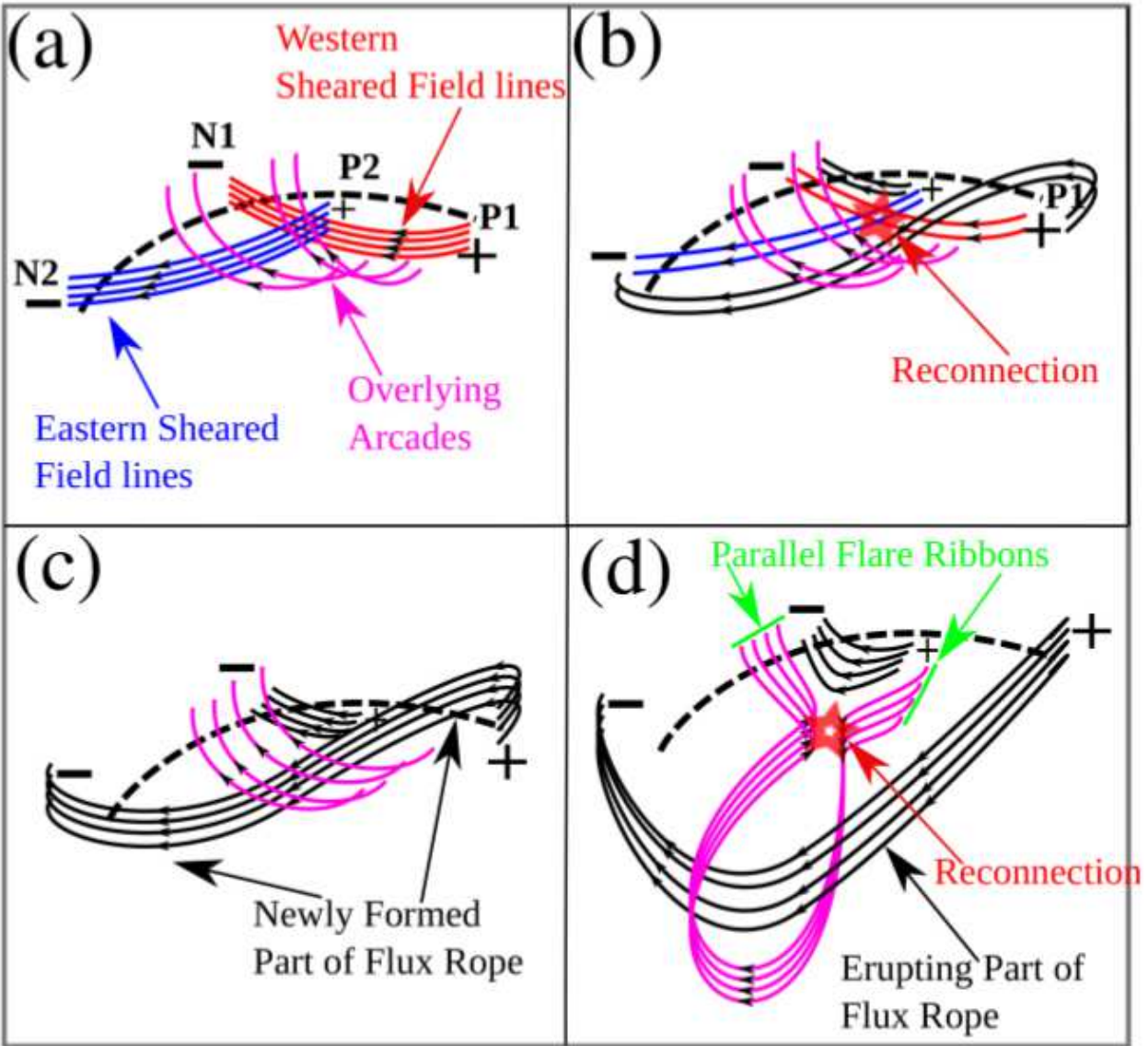


Fig. 9.— Schematic of the flare during the first component of the eruption, which occurs in the northeastern lobe of the huge fan dome; this region corresponds to the green lines in the schematic in Figure 14. The black dashed line shows the polarity inversion line (PIL), the red and blue lines show the impacted sheared field lines that reconnect, the black solid lines represent the magnetic lines formed by the reconnection, and the purple lines represent overlying arcade loops. Red stars in panels (b) and (d) show the reconnection region.

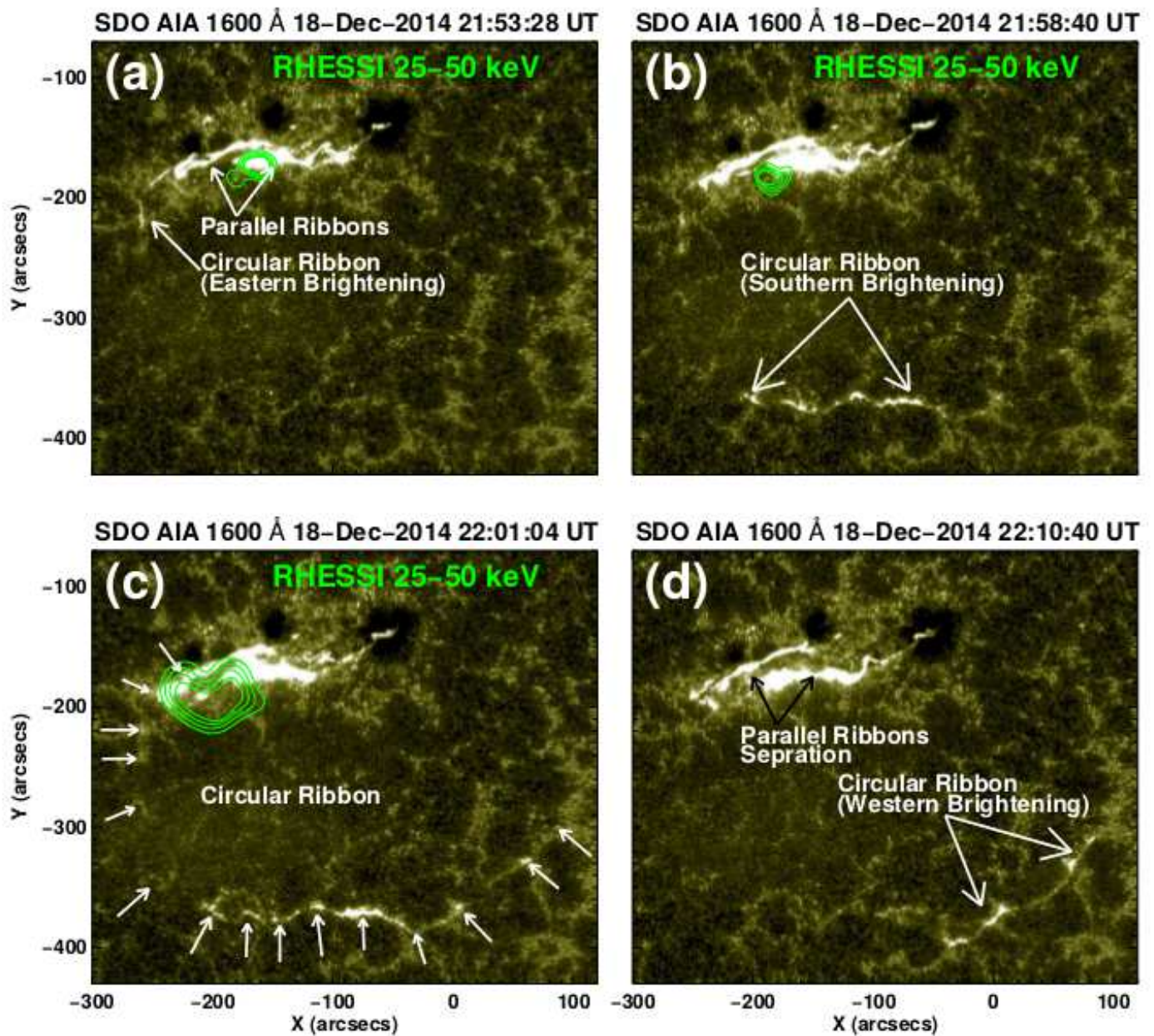


Fig. 10.— Sequence of selected *SDO/AIA* 1600 Å images, showing the evolution of the two-ribbon parallel flare ribbons and the circular ribbon. The green contours in panels (a) and (b) map *RHESSI* X-ray intensity in the energy range 25-50 keV, generated with the PIXON algorithm. The contours levels are 20%, 30%, 40%, and 50% of the peak intensity. The integration time is 20 s.

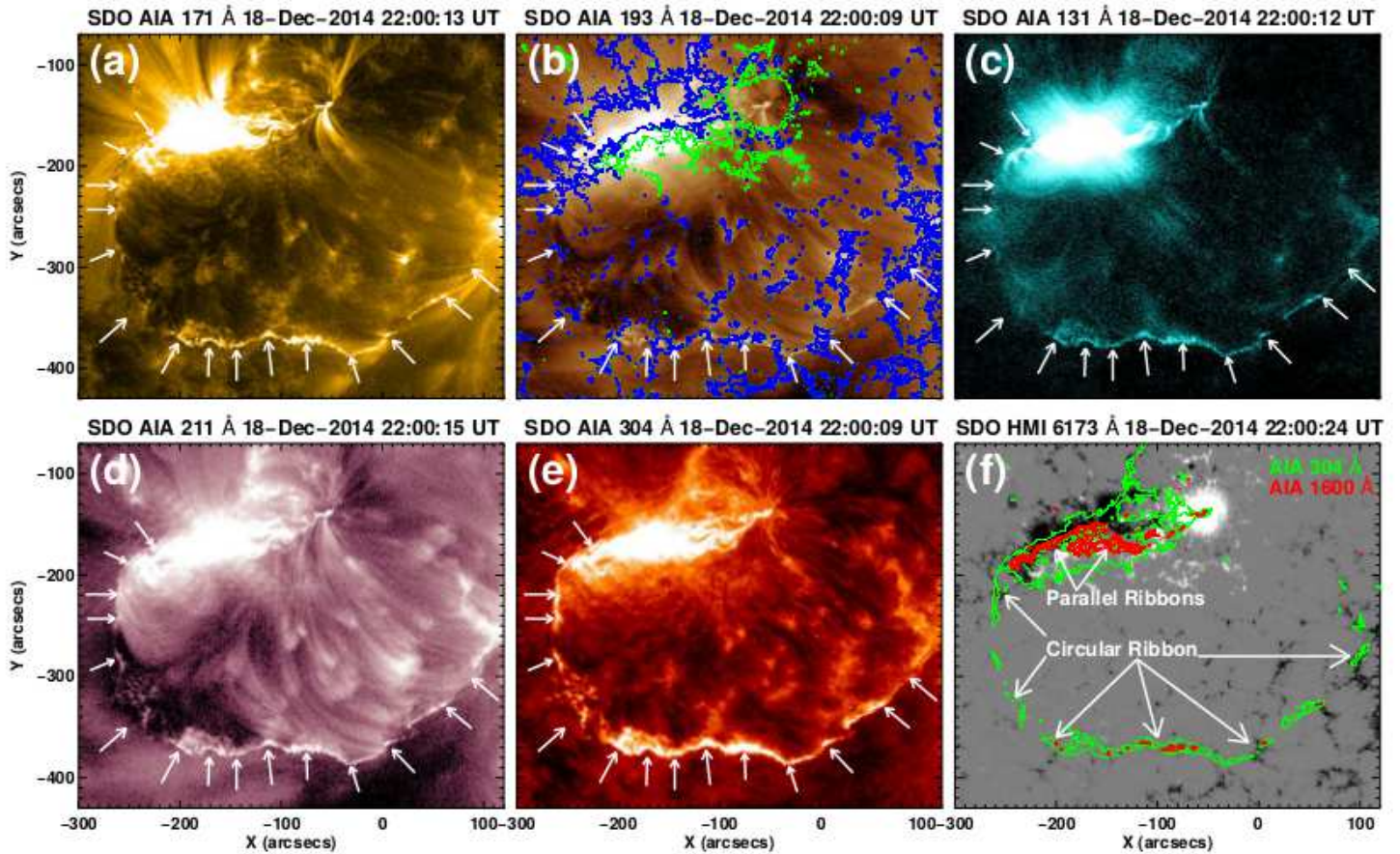


Fig. 11.— *SDO/AIA* 171 (a), 193 (b), 131 (c), 211 (d), and 304 (e) Å images at  $\sim 22:00$  UT, showing the circular ribbon. In panel (b) the blue and green contours show the photospheric magnetic field contours for negative and positive polarity field, respectively, with contour levels of  $\pm 40$ ,  $\pm 50$ , and  $\pm 100$  Gauss. (f) *SDO/HMI* line-of-sight magnetogram at  $\sim 22:00$  UT, with overlaid *SDO/AIA* 1600 Å (red) and 304 Å (green) contours. The contour levels are 5%, 10%, 20%, and 30% of the peak intensities.

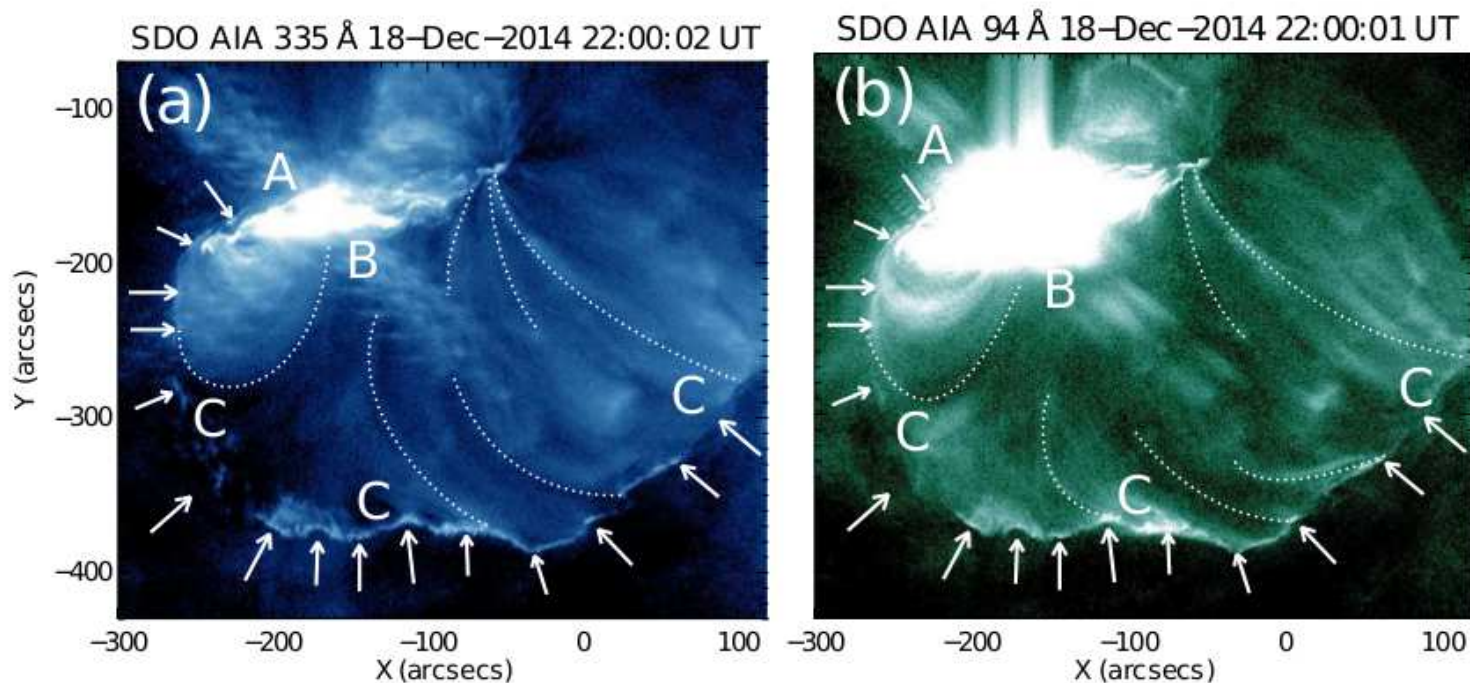


Fig. 12.— *SDO/AIA* 335 and 94 Å images at  $\sim 22:00$  UT showing inner-fan-dome new closed loops made and transiently heated by the null-point reconnection driven by the erupting arcade, which was blown out by the erupting flux rope in its core. The dotted lines show example field lines, and the arrows show the location of the circular flare ribbon, which forms at the footpoints of the transiently-heated portion of the inner-dome field.

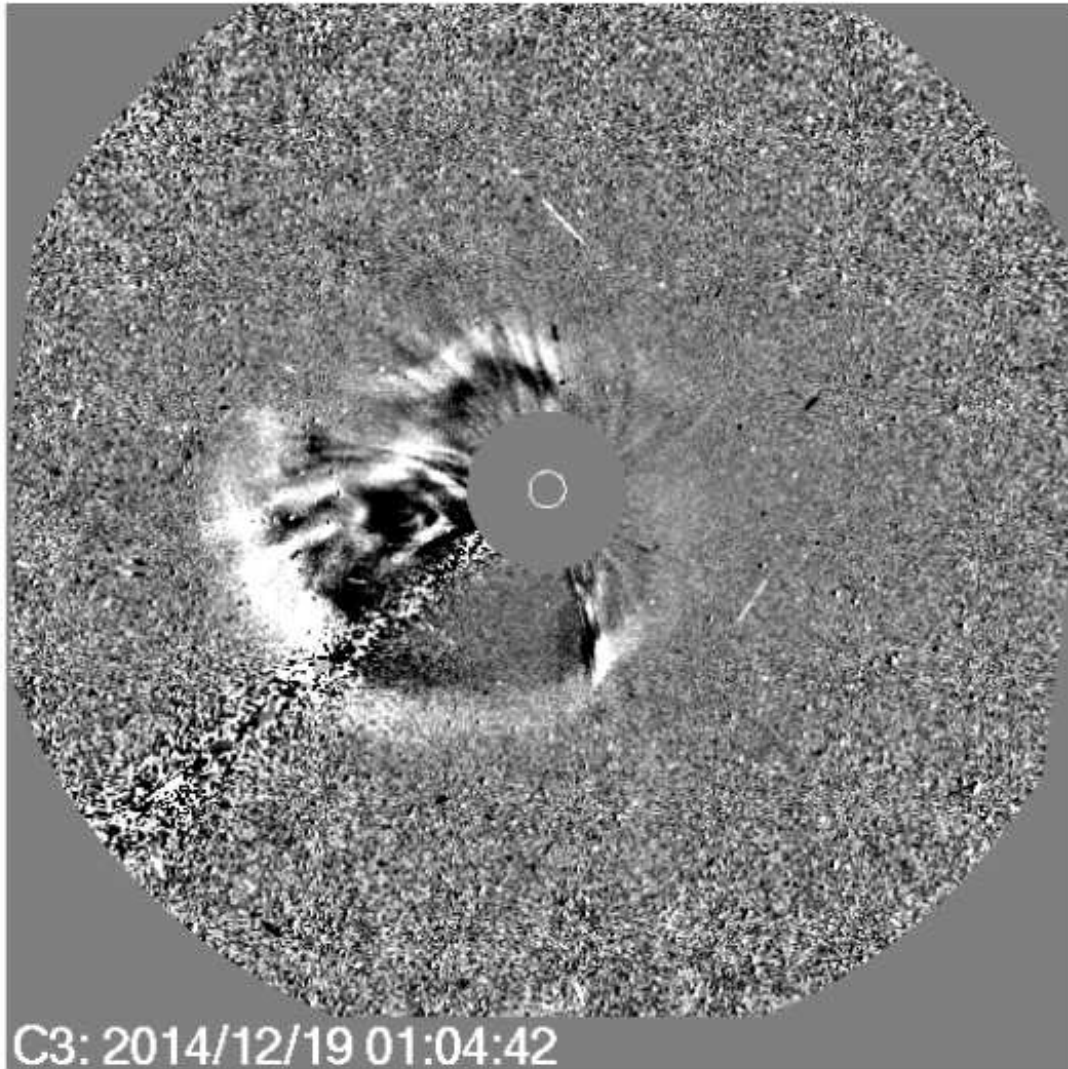


Fig. 13.— SOHO/LASCO C3 coronagraph image at 01:04:42 UT, showing the halo CME produced by the eruptive event studied here. The difference image is collected from *SOHO*/LASCO catalog ([http://cdaw.gsfc.nasa.gov/CME\\_list/](http://cdaw.gsfc.nasa.gov/CME_list/))

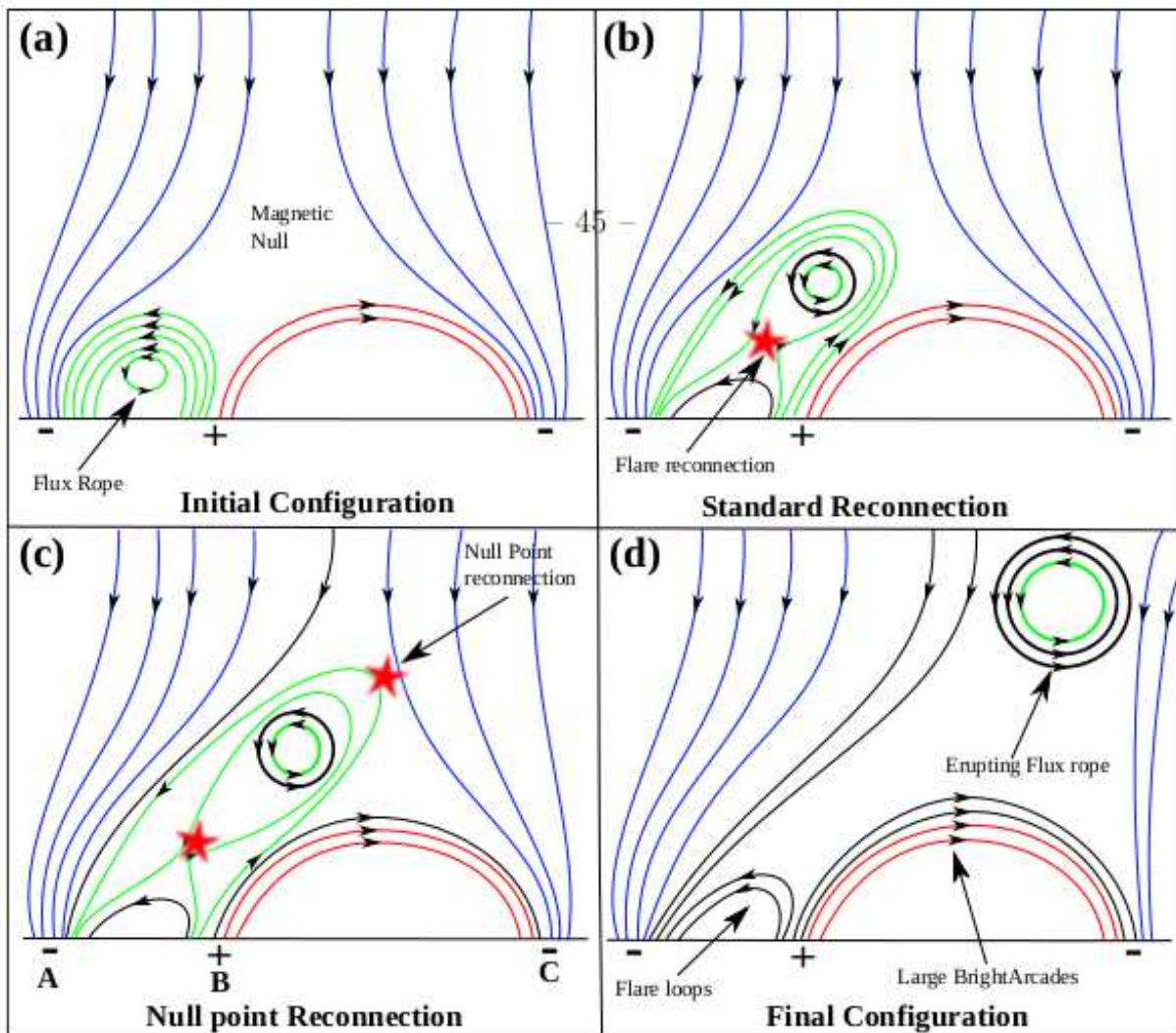


Fig. 14.— Schematic for our large-scale event studied here. Blue lines and open-ended black lines represent field that reaches distant solar locations, or is open. Red and green lines represent the initially closed field lines of the inner shell of the fan dome. Black lines represent field lines formed after reconnection. Red stars mark the reconnection locations. This eruption schematic matches very well with both the large-scale-eruption scenario proposed by [Joshi et al. \(2015\)](#) for a different large-scale eruption, and the jet-formation schematic presented in jet papers by [Sterling et al. \(2015, 2016, 2017\)](#). Panel (a) represents the initial configuration. From the perspective of the 2014 December 18 eruption of this paper, the green field on the left-hand side erupts to produce the two-ribbon flare in the two-ribbon component of the event (Figure 9), with the ribbons forming, between locations A and B (see labels in panel C), due to tether-cutting reconnection. The right-hand-side reconnection corresponds to the null-point-reconnection component of the event, with the newly-formed large-lobe loops between locations B and C corresponding to the new loops made and heated by the null-point reconnection (see Figure 12), and the foot of that bright loop at location C corresponding to one location of the circular ribbon as viewed on a 2D cross sectional plane. From the jet perspective: Panels (b) and (c) show a miniature flux rope erupting, with the tether-cutting reconnection (called internal reconnection in the Sterling et al. jet papers) on the left-hand side (panels b and c) occurring to make a bright structure between locations A and B in (c). This is what Sterling et al. call a jet-base bright point (JBP; a miniature flare arcade having a miniature pair of flare ribbons in its feet in the case of jets). Thus the JBP is a miniature flare, corresponding to the two-ribbon flare of the large-scale event. The null-point reconnection (also called breakout reconnection or interchange reconnection, and called external reconnection in the Sterling et al. jet papers) on the right-hand side (panel (c)) creates new bright closed loops between locations B and C, and also new far-reaching field lines. This reconnection of the far-reaching field results in a heated jet column in the Sterling et al. jet papers.